POLITECNICO DI TORINO

Master of Science in Aerospace Engineering

Master Degree Thesis

Design of a robust nonlinear attitude estimation algorithm for Space Rider mission

Supervisor
Prof. Elisa Capello

Candidato
Vittorio Pistone

Company supervisors
AVIO
Dr. Marco Giannini

Academic Year 2020-2021

Don't panic!

Abstract

An important part of almost every space mission post-launch analysis is the attitude sensors performance assessment. Launch vibrations, orbit insertion and a harsh operating environment could degrade the sensors data reliability. Even mounting errors during vehicle assembly and integration could occur, mining the mission success. Generally, spacecraft attitude sensors require extensive in-flight calibration during their operational life to ensure pointing requirements are satisfied. Continuous on-board calibration also provides a mean for fault prediction and detection trough parameters tracking.

Star trackers are among the most accurate instruments to estimate a spacecraft orientation in space, achieving accuracies to the arc-second range in the boresight pointing direction. Effectiveness and reliability have made this sensor an irreplaceable component for the attitude determination system of large satellites and, as the technology improves and allows the miniaturization of the equipments, even for the small and micro ones. However, in order to maintain high pointing accuracy, it's necessary to account for misalignments, lens distortion and sensor alterations, due by the environmental changes throughout the entire mission envelope.

The main objective of this thesis is to exploit the usefulness of spacecraft dynamic modeling for nonlinear attitude state estimation techniques, investigating the feasibility of estimation algorithms to assess the star trackers misalignments w.r.t their mounting directions. Although the nonlinear nature of the spacecraft dynamics doesn't allow for optimal solution, sub-optimal nonlinear state estimation filters are provided, in order to estimate the vehicle states and compensate for the degrading performances of the inertial sensors. In particular, three filters have been implemented: a Kalman filter in its linear and extended formulation and a variable structure observer based in the sliding mode.

A continuously operating EKF-based calibration filter estimates attitude rate and quaternion orientation, producing optimal attitude solutions, in therms of minimum variance, regardless of the attitude motions. Instead Sliding Mode Observers are typically used for the design of attitude and angular velocity determination algorithms (routines) to reduce the computational load of traditional nonlinear filters but preserving their accuracy and stability.

Space Rider is a reusable unmanned space transportation system, integrated with Vega-C, designed and developed by ESA and European partners to provide a regular access to LEO for several space applications. Space Rider inertial parameters and sensors are implemented in a comprehensive framework in Matlab and Simulink environment and Montecarlo simulations have been performed to test the filters' performances with different initial conditions and scenarios.

Sommario

Una parte fondamentale di quasi tutti tutte le analisi post lancio è la valutazione delle prestazioni dei sensori. Vibrazioni durante il lancio, ingresso in orbita ed un difficile ambiente operativo possono causare la perdita di affidabilità nelle misurazioni dei sensori. Anche errori durante la fase di montaggio potrebbero accadere, mettendo a serio rischio il successo della missione. Generalmente i sensori per l'assetto dei velivoli spaziali richiedono una intensiva calibrazione in volo durante la loro vita operativa per garantire i requisiti di puntamento siano soddisfatti. Un costante processo di calibrazione permette anche di monitorare eventuali parametri critici per prevenire ed individuare eventuali guasti.

I sensori di stelle sono tra i più accurati strumenti per la stima dell'assetto nello spazio, riuscendo a raggiungere un'accuratezza dell'ordine dell'arco-secondo nella direzione di puntamento. La sua efficacia ed affidabilità lo hanno reso una componente fondamentale dei sistemi di assetto di grandi satelliti e, con il progressivo miglioramento della tecnologia, anche per piccoli e micro satelliti. In ogni caso, per poter mantenere un'elevata accuratezza di puntamento è necessario tenere in conto di disallineamenti, distorsioni delle lenti e alterazioni dei parametri dei sensori, causati dalle variazioni ambientali durante l'intero ciclo operativo.

L'obiettivo principale di questo lavoro di tesi è l'utilizzo dei benefici legati all'uso della dinamica del velivolo all'interno degli algoritmi di stima per sistemi non lineari per valutarne l'applicazione nel calcolo dei disallineamenti dei sensori di stelle rispetto ai loro assi di montaggio. Sebbene la natura non lineare della dinamica considerata non consenta l'esistenza di soluzioni ottimali, dei filtri di stima sub-ottimi sono stati implementati per la stima dello stato e compensare il peggioramento della qualità nei sensori inerziali. In particolare sono stati implementati tre filtri: a un filtro di Kalman lineare, uno nella sua formulazione estesa e un osservatore a struttura variabile basato sul modo di scivolare.

Un filtro di calibrazione basato su algoritmi EKF che operano in maniera continua riesce a fornire stime di assetto e velocità angolari, producendo soluzioni di assetto ottimali, in termini di minima varianza, a prescindere dalla dinamica rotazionale. Invece gli osservatori in sliding mode sono tipicamente utilizzati per la costruzione di routine di bordo per diminuire i tipici costi computazionali dei filtri non lineari, ma senza perdita di qualità e stabilità.

Space Rider è un sistema di lancio spaziale senza equipaggio e riutilizzabile, integrato con Vega-C, progettato e costruito da ESA e partner europei per fornire un accesso regolare alla fascia LEO per un'ampia scelta di applicazioni. I parametri inerziali ed i sensori di Space Rider sono stati implementati in un simulatore sviluppato su Matlab e Simulink e simulazioni Montecarlo sono state eseguite per valutare le prestazioni dei sensori con diversi scenari e condizioni iniziali.

Acknowledgements

Contents

List of Tables

List of Figures

List of Abbreviations

ADCS Attitude Determination and Control System
APS Active Pixel Sensor
ARW Angular Random Walk
AVUM Altitude and Vernier Upper Module
AU Astronomical Unit
CCD Charged Coupled Device
CMG Control Moment Gyroscope
CMOS Complementary Metal-Oxide Semiconductor
DoF Degrees of Freedom
ECEF Earth-Centered, Earth-Fixed
ECI Earth-Centered Inertial
ESA European Space Agency
FOV Field of View
GPS Global Position System
JPL Jet Propulsion Laboratory
HST Hubble Space Telescope
KF Kalman Filter
IMU Inertial Measurement Unit
IXV Intermediate eXperimental Vehicle
LEO Low Earth Orbit
LTI Linear Time Invariant
LVLH Local Vertical Local Horizontal
NASA National Aeronautics and Space Administration
QUEST Quaternion Estimation
RIG Rate Integrating Gyroscope
RWS Reaction Wheel System
SPACESTAR Satellite Platform Avionics Computer Embedding ST Algorithms
SMM Solar Maximum Mission
SMO Sliding Mode Observer
SR Space Rider
TRIAD Tri-Axial Attitude Determination System
UKF Unscented Kalman Filter
VSS Variable Structure Systems

Chapter 1

Introduction

Along with the development of Earth observation, deep-space exploration and celestial navigation, attitude measurement requirements and constraints are rapidly increasing. Pointing accuracy is strongly related to sensors' measurement data quality, likely to degrade and accumulate errors during their operational life. In slightly more than half a century of spaceflight, technologies advancements have improved every aspect involved in the spacecraft design, currently pushing towards the achievement of completely autonomous navigation and control in orbit.
In this context, as the new generation computers are capable of executing multiple tasks at the same time in a smaller timeframe, two nonlinear estimation techniques have been implemented to be executed as Space Rider's onboard routines. In particular, this thesis work explores observer-based routines based on Kalman filters and sliding mode observers to localize star trackers frames misalignments w.r.t the nominal mounting directions.

Historically, on board processor limited capabilities have precluded star trackers employment as a primary sensor for attitude determination. Instead gyros were employed as the reference source for attitude and attitude rate determination, occasionally updating gyro drift through star sensors data.
A combination of gyroscopes and star sensors is among the most effective solution to provide an inertial orientation reference. A gyro stabilized platform supplies measurement data even in presence of high attitude rates but it's prone to drift due to integration errors propagation. Instead, star trackers, which lack in high frequency dynamics or during occultation from stars and planets, can be used as a more accurate reference, since its performances are more likely to remain unchanged. However in order to account even for the smallest errors, also star trackers misalignments should be considered.

An important part of post launch analysis for almost every spacecraft is the attitude sensors performance assessment. Typical space qualified attitude sensors

require extensive in-flight recalibration to guarantee pointing error requirements are satisfied. Instruments calibrations can also be used to assess performance trending, failure prediction and detection.
Ground-based calibration is time consuming, costly and prone to error because of the technical personnel required. A huge amount of telemetry data need to be analyzed to verify the calibration parameters and, besides the common bandwidth problems for deep space mission, where data rate is relatively low, this becomes a big problem during mission definitions and subsystems sizing. Limiting ground support to data monitoring and for contingency situations, with in-flight calibration software executions can significantly reduce the costs and improve mission efficiency.

Figure 1.1: Liftoff of space shuttle Columbia carrying Chandra X-ray Observatory on mission STS-93 [1]

Several technical benefits are related to on-orbit calibration, including: more precise pointing accuracy, real-time tracking of geometrical parameters to estimate thermal related variations, less CPU space to reserve for telemetry data, minimal interruption of science activities and observations, greater autonomy and less ground-based support required. For these and other reasons the space vehicles of the future will be able to execute calibration routines fully autonomously with more powerful and sophisticated onboard computers.

Although computer processing capabilities were limited in the last century, on-orbit calibration routines were tested in some NASA mission where pointing accuracy was one of the mission driving parameters: Hubble Space Telescope [2] and Chandra X-ray Observatory [3].
Named in honor of the famous astronomer Edwin Hubble, the Hubble Space Telescope (HST) is a large space based telescope launched with space shuttle Discovery in 1990. Inserted in a Low Earth Orbit (LEO), in the last 30 years Hubble has made more than 1.4 million observations and almost 20000 peer-review science papers have been published. With a wide range of light detectable, that goes from ultraviolet to near-infrared, the telescope has tracked interstellar object in and outside the Solar system, discovered Pluto's moons and captured images up to 13.4 billion light years from Earth. This massive observed distance, from a spacecraft that is just orbiting Earth is really notable. It will be extended up to the limits of the expanding Universe by its successors that will be launched at the end of this year: James Webb Telescope. Hubble is equipped with numerous sensors to provide fine pointing accuracy up to 0.007 *arcsec*, namely: six gyros, two magnetometers, three fixed head star trackers and three guidance sensors.

Figure 1.2: HST view from Atlantis' robotic arm during Servicing Mission 4 [1]

Besides being one of the more science profitable NASA project, Hubble is also special among the other telescope that flew and flies nowadays. Indeed Hubble was the first telescope designed to be visited in space for instruments update and servicing. In-orbit servicing capabilities have been crucial to save the space telescope, since after orbit insertion an aberration on the primary mirror was discovered on the first pictures, drastically affecting the images' quality. Overall, five servicing mission have been executed from the space shuttle's crews.

Chandra X-ray Observatory represents the most important space based observatory to detect X-ray emission from very hot regions of the Universe, tracking exploded stars, cluster of galaxies and hot matter orbiting black holes, up to the last second before it falls inside. It was launched in 1999 by space shuttle Columbia and boosted up to acquire a highly elliptical orbit with an apogee[1] of 139000 km and perigee[2] of 16000 km, where no residual atmosphere could affect measurements quality absorbing radiation in the X-band. This high altitude high eccentric orbit, more than 1/3 of the Earth-Moon distance at apogee, is mandatory for this kind of space telescope and enables the vehicle to stay above the higher layers of the atmosphere for most of its orbit, which lasts around 64 hours and 18 minutes.
Chandra is equipped with a set of sensors capable of achieving a pointing accuracy of 30 $arcsec$ and holding this value for 99% of the observation time. This telescope also stands as the biggest payload deployed by a space shuttle cargo bay with almost 15 meters length in its principal dimension.

Both Hubble and Chandra are two really expensive missions and for this reason every science observation interruption should be avoided or at least minimized to enhance mission efficiency and prevent waste of money. For example, Hubble had to remain in an inoperative mode from 4 to 6 months after each servicing before resuming science operations. Besides extensive servicing operations, performing misalignments estimation and calibration in orbit could radically change space mission perspective, reducing ground support to automated monitoring and trend analysis.
These telescopes belong to NASA's Great Observatories program, funded to build a space asset for astronomy covering every different wavelength, from infrared to gamma rays. Spitzer Space Telescope is the third element of this program and represent the largest infrared telescope ever launched into space. As for Hubble and Chandra, Spitzer regularly executes attitude estimation routines to detect necessity for sensors' calibration.

Calibration algorithms performance are measured by means of multiple parameters, in which execution time and reliability are among the most important. For

[1]Apogee refers to the point in orbit where the spacecraft is farther from Earth

[2]Perigee refers to the point in orbit where the spacecraft is closer to Earth

Davenport's algorithms and other similar a long inertial hold period and a sequence of control maneuvers are required, lasting several hours, or days, and reducing mission efficiency. Instead, Kalman filters based algorithms can be performed with different maneuvers, do not need long hold period and generally last around 1 hour.
In order to satisfy mission pointing requirements, a reliable real-time calibration algorithm is required. It should comply with the space qualified flight computers capabilities and daily schedule. Moreover, for completely autonomous calibration, the initialization of the process should be triggered following the trends of different parameters, such as: measurement residuals, targeting error and error covariance.

Figure 1.3: Chandra X-ray Telescope deployment from Columbia's payload bay [1]

However, despite significant improvements have been made to automate ground-based calibration, several impediments occurred and prevented on-orbit calibration becoming a standard tool in space mission. To mention a few, the development costs and the technical challenges of relatively new calibration algorithms are not negligible, these filters are often computationally intensive for S/C on-board computers.

Indeed, until the last decades, attitude estimation algorithms were performed by large mainframe computers on the ground.

1.1 Literature Review

The development of precise sensors for space-based application made it clear that multiple noise sources could mine the measurement data reliability, thus leading to the study of statistically optimal filters, firstly described by Wiener in 1940. His work lead the way from classical control theory and signals processing to the modern control theory and estimation.

Since attitude determination and estimation are often improperly used, some important differences should be highlighted. Attitude determination refers to approaches that compute attitude without any information about sensor noise statistical properties. Instead attitude estimation uses the attitude dynamic model to propagate the satellite orientation and integrate filtered measurements.
Attitude determination approaches can be divided in two categories: attitude dependent and independent. The first one includes static attitude determination and refers to memoryless approaches that determine the attitude point-by-point in time, which require a certain volume of data to fully provide the attitude solution. The second one comprises attitude estimation algorithms trough filtering approaches to predict the state evolution during time, given the S/C dynamic model and a series of measurements provided by the sensors [4].

Each of these categories can be further divided into batch estimators and filtering or recursive and sequential methods [5]. A batch estimator update the state vector at at a fixed time, using a set of observations collected during a defined timeframe. Instead sequential estimators update the state vector after each measurements set. The two main components of sequential estimators are recursive least-squares estimators and Kalman filters. Since batch and recursive least-squares methods do not include process noise because of the implementation difficulty in a least-squares algorithm, they are not suitable for real-time calibration. On the other hand, filters generally provide optimal attitude solution but proper initialization is required to guarantee convergence. Besides being capable of solving lost-in-space problems without a priori attitude information, filtering can generally provide a more accurate estimate than static methods because it keeps memory of past measurements and improves the solution at each integration step.
Both static and filtering approaches have advantages and disadvantages. The main advantage of static approaches is that a solution is always provided with at most a very rough a priori estimate of the desired quantity. Also, these approaches are usually computationally more efficient than filtering approaches. The main disadvantage of static approaches is that full observability is required at each time

frame, so that algebraic singularities do not exist in the solution. Also, some variables cannot be included or determined from a static solution. Finally, optimally combining measurement data with the proper statistical balance may be difficult to do using static approaches.

The branch of in-flight sensors calibration has been studied for several years in many aerospace research projects. The necessity to maintain a high reliability of the sensors' data and the increasing precision demanding during pointing has pushed the scientific community to develop routines for in-orbit sensors calibration.
R.Bellman and R.E. Kalman drastically changed the perspective of this field, reformulating the problem trough differential equations and state space models. Since its publication in a document of *NASA Ames Research Center* during feasibility studies for navigation and control of the Apollo space capsule [6], Kalman filter in its various forms has become a fundamental tool for analyzing and solving a broad class of estimation problems. Even if the first Kalman filter formulation was not suitable for space based application, it became clear that the linear filter theory combined with the linear perturbation concept, already applied in guidance and navigation, was a potential solution to spacecraft's nonlinear navigation problems. Kalman filters' popularity comes from its flexible approach that can generate good solutions to a wide range of estimation problems. Attitude estimation methods based on Kalman theories obtain the optimal state parameters by establishing the state equation and measurement equation of filter system. These solutions become optimal for linear problems with white Gaussian noise sources. The Kalman Filter theory greatly promoted the development of navigation technology combined with star tracker and gyro capabilities.

James Farrell [7] published the first acknowledged paper about Kalman filters for spacecraft attitude estimation, although some works have been previously carried out but not spread because of their national aerospace and defense applications. Farrell studied an Euler angles based formulation, evaluating the feasibility of Kalman filters to provide pointing accuracy with crude measurements from magnetometers and sun sensors, in a torque free environment. Potter and Vander Velde [8] applied Kalman filter theories to obtain an optimum solution for gyroscope and star tracker data fusion. Some applications of sequential filters where also implemented in some routines on the lunar module autopilot.

Multiple attitude representations have been implemented in the filters models. Direct cosine matrices offer a simple approach but routine and truncations errors could cause the matrix to become non orthogonal. Some procedures have been developed to deal with this possibility but require computationally expensive matrices operations. Euler angles formulations are simple and easy to manage but involve nonlinear trigonometric expressions and present some undefined orientation.

The nonsingular quaternion formulation is among the most used attitude representation and it was used in a first application for spacecraft attitude estimation by E.J. Lefferts [9].
Kalman filters with an uncoupled axes quaternion formulation has been employed in some NASA missions such as the International Ultraviolet Explorer and Solar Maximum Mission (SMM).

The Kalman filter is basically a recursive estimation technique that estimates the actual state trough sensors' measurements and space system models, linearized around a working point. This necessary linearization precludes the filter to converge in presence of highly nonlinear systems. To address this weakness, a nonlinear extension of the filter was developed: the Extended Kalman Filter (EKF). The fundamental difference is that while the linear filter linearizes around the initial point, the latter performs linearization on the estimated state at every iteration step. The first published paper about EKF was proposed by Anderson and Moore [10], since then it became the most widely used nonlinear recursive filtering method in the field of attitude determination.
EKF-based algorithms for calibration have found wide interest in the scientific community, as reported in [11]. Their feasibility for in-orbit real-time calibration has been demonstrated on two NASA spacecraft: Spitzer Space Telescope [12] and Cassini [13]. Both softwares have been developed by the Jet Propulsion Laboratory (JPL) and performed every four days and at least twice per year, respectively.
However, the nonlinear state equations and the measurement equations of the EKF method may lead to biased state estimation or even filtering divergence because of local linearization approximation in the vicinity of the state prediction.

Besides the linear and extended Kalman filters, other alternatives have been introduced, such as the Unscented Kalman Filter (UKF), also referred to as sigma-point filters, and particle filters. Unscented filters [14] estimate mean and covariance of the state vector trough second higher-order approximations of nonlinear functions distribution, avoiding the EKF drawbacks for highly nonlinear systems. However unscented filters are unable to represent a general probability but only a Gaussian distribution. Particle filters could offer a solution to this problem taking into account multiple probability distributions [15].

Some years later of R. Kalman work on filters for noisy systems as a tool in linear estimation theory and its application to nonlinear orbital guidance and navigation problems during the Apollo program, several other related studies were carried out. The dawn of attitude estimation can be found in the work of Black, who developed the *algebraic method* for the point-by-point determination of a spacecraft's attitude from a set of two vector observations in 1964. Shuster renamed the algorithm TRIAD (Tri-Axial Attitude Determination System) in an IBM internal report [16].

Just one year later, Grace Wahba published her works about attitude determination from any number of vector observation [17]. However the first solution to Wahba's problem never found a practical application.
Instead, the first practical solution of Wahba's problem was developed by Paul Davenport *q method* [18]. It has been used as the main Inertial Measurement Unit (IMU) calibration tool on many spacecraft for more than two decade. The principal drawback of this algorithm was the necessity to perform an eigenvalue decomposition of a $4x4$ matrix: a serious problem for the on-board computer capabilities of the last century. To solve this problem, Shuster developed the *Quaternion Estimator* (QUEST), which avoids the eigenvalue/eigenvector decomposition. QUEST was the first algorithm to be suitable for on-board computer processor and it's still used nowadays.

The previously described techniques apply to static estimation problems, i.e. when the elements to be estimated remain constant, or at least bounded by some known values. However, when the state is varying in time, attitude estimation trough filtering approaches is required to estimate the state of a dynamic system. Two main strategies can be performed to provide the best estimate of the system state:

- *Filtering approach*: Using a dynamic model and measurements that are both corrupted by random noise of known statistics the filter acts to minimize a loss function in order to provide the best estimate of the state vector.
- *Observation approach*: The observer is a mathematical replica of the system which estimate the unmeasurable states of a system. The algorithm performs a recursive correction of the state estimate driving the error between the measured system and the observer output to zero.

Historically, attitude and navigation filters have been implemented using only the kinematic relations to reduce the state vector size and thus the computational load but fail to provide a valid attitude solution in certain operative conditions. The inclusion of dynamic equations of motion, besides requiring a larger state space model and thus a higher computational load, could increase the probability to introduce model uncertainty, potentially degrading the output data reliability.
In this thesis, the attitude estimation filter design includes spacecraft rigid body dynamics and disturbance torques.
Dynamic model inclusion has been investigated by several authors, in particular when the measurements data quality result to be low or the amount available is not enough to provide a valid attitude solution [19] [20]. In one study, Crassidis and Markley employed dynamic modeling for spacecraft attitude estimation in the complete absence of rate gyros [4].
Yang and Zhou [21] developed an EKF formulation with incorporated dynamic showing it has better performance than the same model without S/C dynamic

since it's implemented with a larger set of data. This model also avoids the singularity issue in the covariance matrix, using a quaternion reduced model.

In order to evaluate the performance of the EKF, a nonlinear variable structure technique for state estimation is also presented: the Sliding Mode Observer (SMO). In sliding mode control, Variable Structure Systems (VSS) are designed to drive and constrain the system along a precise dynamic.
Sliding Mode Observers are nonlinear state estimators whose development stems from the theory of Variable Structure Systems (VSS), a field of study initially applied as a robust control method. Sliding mode techniques evolved mainly thanks to the pioneering work of the Soviet Union in the 50' and 60', based on the works of Pointcarè and Lyapunov. The first publication in English language was made by Vadim Utkin [22], a Ph.D holder from Moscow Institute for Control Sciences who moved in the USA at the end of the '70.

Several works about controller and observer based in the sliding mode for three-axis attitude stabilization have been proposed, with focus on nonlinear state estimation by mean of sliding surfaces. Drakunov [23] has been the first to analyze the observer performances in a stochastic mathematical environment, while Slotine [24] and Misawa [25] extended it to a deterministic framework, also providing an extensive review on the topic.
A decoupled sliding mode controller and observer has been described in the paper by James H. McDuffie and Yuri B. Shtessel [26] [27]. A similar design with additive and multiplicative quaternion correction to estimate angular rate trough sliding mode observer was given by Kerem Köprübasi and Win L.Thein [28]
Salcudean presented a globally convergent, nonlinear, discontinuous observer for rigid body motion using quaternions for the orientation measurement [29].

In opposite to the EKF that requires time-varying gains, to be evaluated at each iteration step and thus resulting in a high computational demand for the onboard spacecraft computer, the presented formulation of SMO requires only two set of fixed gains (Luenbergers' and switching gains).
Sliding mode technique results to be suitable for observer problems thanks to its ability to produce a set of estimate variables highly commensurate with the actual system state. They also guarantee robustness to modeling uncertainty and unknown bounded disturbances. The main drawback is the chattering of the state estimates because of the definition of the sliding surface by mean of the saturation or signum function.

1.2 Overview of Space Rider

Space Rider (SR) is a un-crewed and reusable end-to-end integrated space transportation system [30], developed by the European Space Agency (ESA) from the flight experience of Vega and the *IXV Experimental Vehicle (IXV) project*. The IXV vehicle was launched for the first time in February 2015, performing an overall flight of roughly 25000 km, including autonomous atmospheric reentry from an orbital velocity of 7.5 km/sec ($Mach = 27$), smooth touchdown and precision landing.

The heritage of this mission has been fully embedded in the Space Rider program to provide an affordable access to space for a wide range of in-orbit application, from microgravity laboratory experiments to rendezvous and capture of other bodies. Its reduced payload's integration time and early recoverability after reentry offer a cheap solution to the current space transportation possibilities.
Space Rider is launched atop the Vega-C rocket from ESA Spaceport in Kourou, French Guyana, and will stay in orbit 2 months or longer prior to reenter in atmosphere and land. The landing site varies in function of the orbit inclination, likely to be in Santa Maria in the Azores archipelago (Portugal) or French Guyana and Dutch Caraçao for inclinations higher and lower of 37°, respectively. The reference mission for SR is a circular orbit with an inclination of 5° and an altitude around 400 km but higher inclination and altitude are exploitable.

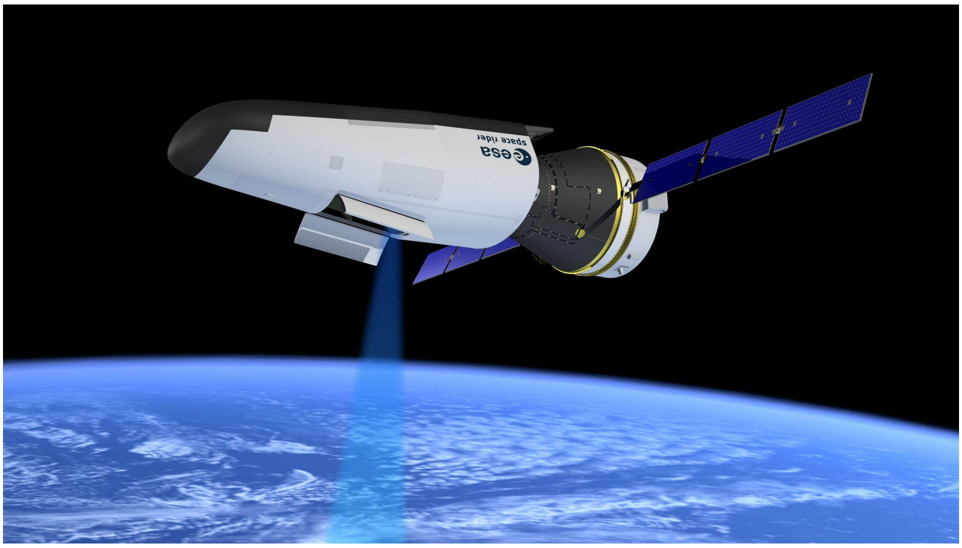

Figure 1.4: Space Rider rendering in its nominal attitude [30]

Fully integrated with the Vega-C Launcher System, SR provides an independent robotic laboratory in Low Earth Orbit (LEO) for a wide variety of applications besides Earth observation, with accurate pointing capabilities, in particular for Nadir

and Zenit directions.
Micro-gravity experiments, including pharmaceuticals, biomedicine, biology and physical science can be conducted in the environmentally controlled bay, with a cargo volume up to 800 m^3. SR also offers a solution for in-orbit demonstration and validation of new technologies, such as robotics and debris removal, with the possibility to perform in-orbit satellite inspections.

Space Rider is composed by the following modules:

- *SR-AOM*: the AVUM Orbital Module. It's a modified version of the Vega C upper stage, that provides power, telemetry, thermal and attitude control to the entire system, and stores the tanks for propellent or other liquids. It ensures the initial orbit insertion and boost the reusable module to acquire the re-entry interface before detaching and burning in the atmosphere.
  The Attitude and Vernier Upper Module (AVUM) has a bi-propellant main propulsion to provide orbital injection to Vega's last stage and a mono-propellent secondary propulsion system for roll and attitude control. The SR-AOM is equipped with an AVUM Life Extension Kit (AVUM + ALEK) which enables the vehicle to orbit for more than two months, where ALEK is a new concept of scalable space module developed by AVIO for Vega launchers.
- *SR-RM*: the Re-entry Module. It's a modified and reusable version of the IXV, equipped with a Multi-Purpose Cargo Bay with a field of view ranging from Earth to Deep Space. It lands, refuels and it's ready to be launched again in 180 days. Its design has been driven by the necessity of maximize the payload's volume available for instrumentations. Several configurations and box division are provided, with the possibility of compartment pressurization, isolation and Earth-orientation of the payloads.

After atmospheric reentry, a two stage descent system drastically reduces the vehicle's speed to prepare for landing. The first stage is a pilot + drogue parachute that slows down Space Rider to the nominal opening speed of the second descent stage: a driving parafoil.
Actually the maiden flight is expected to be in the first quarter of 2022.

1.3 Attitude Hardware

Attitude determination is the process of estimating the orientation of a spacecraft with respect to a fixed reference frame trough one or multiple on-board observation. Combinations of these observations are used to improve the estimates' accuracy of spacecraft rotational attitude. Several space qualified sensors exist, each of them providing attitude information from different sources, including: sun sensors, Earth horizon sensors, three-axis magnetometer, star trackers, rate integrating sensors and

Figure 1.5: Reference mission timeline for Space Rider [30]

global positioning sensors (GPS).
In this section an overview of the most widely used attitude sensor is presented:

Star trackers: measure star coordinates and brightness to determine the spacecraft orientation in space, tracking multiple stars simultaneously and matching them with an internal catalog in real time. Typically these devices have a mass up to 3 kg, a power requirement around $10 - 20$ W and an update rate between 0.5 Hz and 10 Hz, depending on the current attitude dynamic of the spacecraft. As computer processor technology improves, the sampling frequencies will increase, achieving a higher data accuracy. State-of-the-art star trackers basically consist in a digital camera with wide field of view focal plane (typically up to $8° \times 8°$). Starlight is captured either from CCD (Charged Coupled Device) or CMOS (Complementary Metal-Oxide Semiconductor) pixel technologies. The first provide cleaner data with lower noise while CMOS based sensors feature the advantages of microprocessors and are more resistant to a radiative environment. Some of the most recent optical technologies include the capability of raw data processing on the focal plane itself, known as APS (Active Pixel Sensors).

Star sensing and tracking devices can be divided into three upper classes [5]:

- *Star scanners*: which do not have moving parts and use the spacecraft rotation to provide stars searching and sensing data. Used on spinning spacecraft, light from stars in the FOV passes trough multiple slits and provides a valid attitude solution after several passages. Accuracy is between the lowest among this type of sensor, ranging from 0.5 *to* 30 $arc - minutes$.

- *Gimbaled star trackers*: which allow for 3-axis control using a mechanical support. The optical FOV is small (less than 1°) but the gimbals give the sensor a larger effective FOV. Typical accuracies range from 1 *to* 60 *arcsec*.
- *Fixed head star trackers*: which have electronic searching and tracking capabilities over a certain field of view (FOV). This type of star sensor is smaller and lighter than the previous one and has no moving part.

Obviously, star sensors high performances do not come without drawbacks: they are heavy, expensive and require more power than other attitude sensor. Their accuracy is strictly related to their position on the spacecraft since thrusters' plume, occultation and interference from other bright bodies can degrade their data reliability. Stray light is also a major problem, usually faced with particular coating over the optical sensor to minimize the exposure of the optical system. Furthermore an intensive study is required to correctly obtain data from this sensor: for example, even the most accurate star sensors are unable to determine spacecraft's attitude if the vehicle is rotating too fast. As a consequence, in order to achieve stability and enable the sensor to resume tracking the stars, another type of attitude sensor will be required. High level radiation hardening is also mandatory to avoid failure in case of strong magnetic storms or if the vehicle orbits particular region of the Earth[3].

Gyroscopes: are inertial sensors that measure angle and angular rate from an inertial reference. Mechanical spinning gyros, optical gyros, laser gyros are between the most used. Gyros are generally divided in two main categories:

- *Rate Gyros* (RG): which measure angular rate. These are the cheapest and lightest solution and are subjected to errors caused by drift and nonlinearities.
- *Rate Integrating Gyro* (RIG): which also provide measurements integrating attitude rate or angular angular displacement.
- *Control Moment Gyros* (CMG) can be also used to generate control torques.

Two main solutions are used to design an attitude determination system composed by a set of gyroscopes. The first one aims to keep the gyros rotating axes constantly aligned with an arbitrary inertial frame using a *gimbaled platform*: while the S/C rotates, the gimbals rotate the gyros to maintain the inertial fixed alignment. In this case the orientation between the vehicle and its onboard gyro platform

[3] There is a region over the South Atlantic ocean where the Earth's magnetic field is weaker than everywhere else and Van Allen radiation belt penetrates much deeper in the atmosphere, dipping down to an altitude of 200 km

changes as the S/C undergoes attitude motion. The second design is a complete different solution: gyros are rigidly mounted to the vehicle body in a so called *strap-down* inertial system, therefore providing measurement directly in body frame. In this case no hardware or control components are needed to maintain the original instrument orientation.

Inertial measurement unit is an essential part of every vehicle's guidance and navigation hardware. It's typically constituted by different kind of sensors, such as gyroscopes and accelerometers, and magnetometers for some application, mounted in specific position w.r.t the principal body axes. A typical accelerometer exploits elastic materials to measure linear acceleration, from which velocity and position can be obtained time-integrating. Because in a tridimensional space a vehicle needs at least 6 DoF to fully describe its dynamic. As a consequence, a minimum of 3 accelerometers and 3 gyros are needed to provide valid measurement data. A reliable sensor system would likely contain more sensors for redundancy purposes.
The main drawback on the IMU application is that it typically suffers from accumulated error that propagates during integration and creates drift in the system.

Sun sensors: are visible light or infrared detectors that measure the angle between the incident sunlight and their mounting base. They represent a cheap and light low accuracy solution for attitude determination purposes. Usually some sun sensors are used in the attitude determination systems to provide multiple estimates and increase the overall system pointing precision. Sun sensors can achieve accuracy of 0.01° but require clear fields of view. To guarantee clear FOVs, sun sensor are generally mounted near the ends of the S/C. A slightly improved solution is represented by coarse sun sensors, which are equipped with small solar cells, offering a solution for space mission with a limited power budget.

Horizon sensor: also known as Earth sensors are infrared devices that can sense the temperature difference between the relatively hot atmosphere and the cold of deep space. Atmosphere limits detection provides Earth-relative attitude data with accuracies ranging from 0.1° to 0.25°. However this kind of sensor is limited to applications where spacecrafts orbit planets with a sufficient dense and warm atmosphere.

Magnetometers: are another simple, reliable and lightweight widely used sensor for S/C orbiting around planet which have a sufficiently strong magnetic field, as the Earth does. Magnetometers provide attitude data relative to the local magnetic field orientation but with accuracies among the lowest of the space qualified sensors. Magnetic field orientation and magnitude data can be also combined with magnetic field models preloaded on the onboard computer.

GPS receivers: are high-accuracy navigation sensors usually employed to determine the position in space. But they can also provide attitude information: if the space vehicle is large enough to house more than one receiver with a known distance from each other, the different signals' properties can be used to compute the S/C orientation.

The combination of gyros with star trackers provides a very effective solution for a three-axis attitude determination system. Gyros can be used to update the vehicle orientation for initial stabilization and during interference by sunlight, moonlight or the planet's albedo, while star trackers provide a much higher accuracy attitude data and with respect of an external reference.

1.4 Thesis Organization

This thesis work is organized in the following sections:

- *Chapter 1*: The first chapter has provided a brief introduction on the thesis topic, citing some of the most remarkable works conducted in this framework. Attitude hardware and space-based sensors are also described.
- *Chapter 2*: Overview of reference frame systems, Euler angles and quaternions attitude representation. Description of spacecraft attitude dynamics and kinematics for rigid body spacecraft. The space environment is also described with focus on disturbance and control torques acting on the vehicle.
- *Chapter 3*: The state-space model is introduced. Linear and nonlinear estimation techniques and algorithms are introduced. Sensors modeling and mathematical framework are also described.
- *Chapter 4*: A comparative study is presented between linear and extended Kalman filters and Sliding Mode Observer for a series of numerical simulations.
- *Chapter 5*: Conclusions are summarized and future researches are analyzed.

The goal of this thesis is to exploit different estimation algorithms to track attitude propagation and identify eventual star tracker misalignments in respect of their mounting directions. Each algorithm is evaluated trough multiple variables, such as steady state error, time of execution and data reliability. Controller performances are also tested with every estimation solution.
For practical purposes vectors are not represented with over arrows but in bold characters, at exception of the filtering section.
Finally, although attitude and orbit dynamics are highly coupled, this study only concerns rotational dynamics.

Chapter 2

Spacecraft Attitude Model

In this chapter some useful reference frames and a valid spacecraft attitude formulation are introduced.
The motion of a rigid spacecraft is uniquely identified by its position, velocity, attitude and attitude rate. Position and velocity are determined by the orbital mechanic parameters, such as altitude, orbit inclination and eccentricity. On the other hand, attitude and attitude motion describe the orientation of the spacecraft with respect to a fixed reference frame. Spacecraft attitude determination provides the angular displacements between the two frame, trough one or multiple rotations. In order to fully describe its dynamics six degrees of freedom need to be considered.

2.1 Reference Frame

Based on the type of mission, the spacecraft attitude represented in body frame will be aligned with one or more desired frame. Spacecraft centered and non-spacecraft centered systems are two common categories of reference systems trough which the spacecraft's dynamic can be described. The first category is mainly used in orbital dynamic models, while the latter is proper of attitude dynamic models.

2.1.1 Earth-Centered Intertial Frame

The Earth-Centered Inertial (ECI) frame is used to describe orbital and attitude dynamics. This frame is defined relative to the Earth rotation axis and its orbital plane around the Sun, the ecliptic.
It's center lies in the Earth's center, the $\mathbf{X}_{eci} - axis$ points toward the vernal

equinox[1], the $\mathbf{Z}_{eci}-axis$ intercepts the North Pole, aligned with the Earth's rotation axis, and the $\mathbf{Y}_{eci} - axis$ is oriented in order to complete the direct triad and therefore lies in the equatorial plane.
Because of the Earth motion around the Sun, ECI frame is not inertial but represent a valid approximation for a wide range of studies.

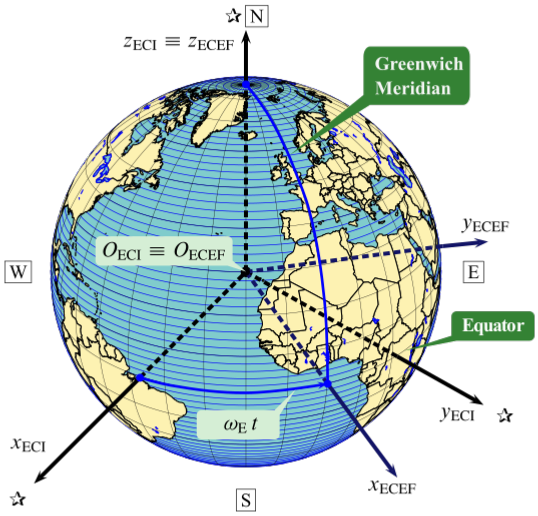

Figure 2.1: ECI reference frame [31]

Strictly related to the ECI frame, the Earth-Centered, Earth-Fixed (ECEF) has the same origin and the same $Z - axis$ direction and versus, $\mathbf{Z}_{ecef}$, thus pointing the north pole. The $\mathbf{X}_{ecef}$ points towards the intersection between the Greenwich Meridian and the equator plane. Finally $\mathbf{Y}_{ecef}$ completes the direct frame following the right-hand rule.

2.1.2 Local-Vertical Local-Horizontal reference frame

The local orbital frame, also referred to as Local-Vertical/Local-Horizontal (LVLH) frame, is used to describe the vehicle's orientation or the relative motion between two bodies.
It's origin is located on the satellite centre of mass, $\mathbf{X}_{lvlh}$, or $\mathbf{V}_{bar}$, is directed along the tangential component of the orbital velocity, $\mathbf{Z}_{lvlh}$, or $\mathbf{R}_{bar}$, points towards the center of the earth, i.e. towards Nadir. Finally, $\mathbf{Y}_{lvlh}$, or $\mathbf{H}_{bar}$ is normal to the orbital plane to complete the direct triad.

[1]The vernal equinox define one of the two points of intersection of the Earth's equatorial plane with the plane of the Earth's orbit around the Sun

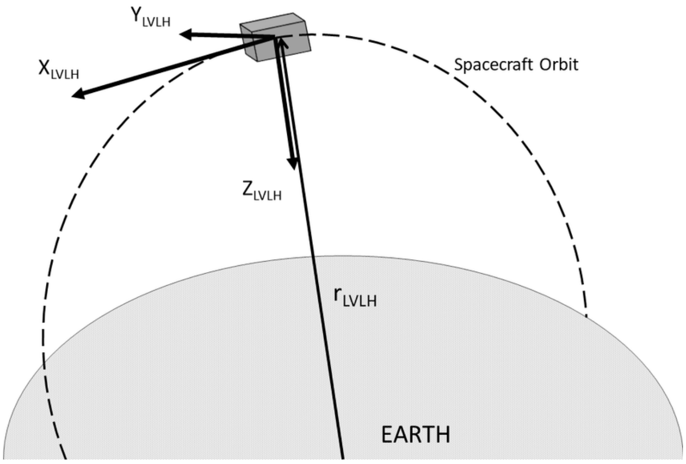

Figure 2.2: LVLH reference frame [32]

A distinction between the local frame and the classic Earth-Centered Inertial frame should be pointed out: the local frame is rotating and therefore non inertial, instead ECI may be considered stationary for several space applications.
Moreover, since $\mathbf{X}_{lvlh}$ and $\mathbf{Z}_{lvlh}$ axes must track the velocity vector and nadir direction, respectively, it follows that the local frame actually rotates w.r.t the ECI frame. In particular $\mathbf{X}_{lvlh}$ and $\mathbf{Z}_{lvlh}$ axes remain in the orbit plane and rotate around Y axis that remains invariant along the orbit.
Therefore the angular velocity of the local frame w.r.t the inertial frame is expressed as

$$\boldsymbol{\omega}_I = \begin{bmatrix} 0 \\ -\omega_{orb} \\ 0 \end{bmatrix} \tag{2.1}$$

where the negative sign derives from the right hand rule and ω_{orb} is the mean orbital velocity calculated as:

$$\omega_{orb} = \sqrt{\frac{\mu}{\mathbf{R}^3}} = 0.0011\ rad/sec \tag{2.2}$$

where μ is the Earth gravitational parameter and $\mathbf{R}$ is the body distance from the Earth's center and whose value is:

$$\mu = GM_{\oplus} = 3.986 \cdot 10^{14}\ m^3/s^2 \tag{2.3}$$

where $G = 6.674 \cdot 10^{-11}\ m^3/(kgs^2)$ is the gravitational constant and $M_{\oplus} = 5.9724 \cdot 10^{24}\ kg$ is the mass of the Earth.
Since this frame is always aligned with its Nadir pointing $Z-axis$, body attitude

knowledge with respect of LVLH is equivalent of having knowledge with respect of the ECI frame.

2.1.3 Body-fixed reference frame

In relation to a spacecraft attitude determination and control system, the first useful frame is the one which enables to describe attitude and attitude rate w.r.t the body axes.
The roll axis, $\mathbf{X}_a$, pitch axis, $\mathbf{Y}_a$ and yaw axis $\mathbf{Z}_a$ define the orientation of the vehicle and are perpendicular to each other.
Rotations around these axis are defined as *roll*, *pitch* and *yaw* respectively.

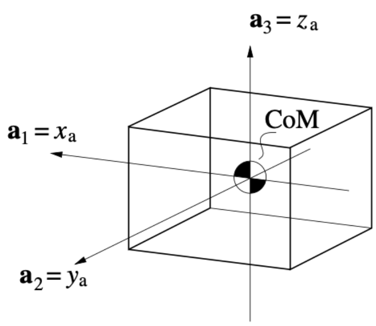

Figure 2.3: Body-fixed reference frame [33]

2.1.4 Spacecraft Geometric Frames

The last coordinate frames presented are essential to describe translation and rotation of the spacecraft w.r.t position and orientation of equipments, such as sensors, robotic arms, thrusters or docking mechanism.

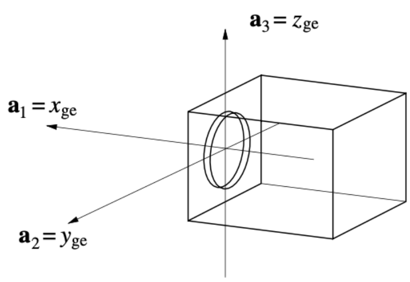

Figure 2.4: Spacecraft geometric reference frame [33]

The frame origin lies in a particular point on the spacecraft body, i.e. the location

of a certain instruments whose orientation is to be parameterized with respect to the body frame.
In this thesis the geometric frame has been used to define the orientation of the on-board star sensors. Here the $\mathbf{X}-axis$ is aligned with the sensor boresight direction, the $\mathbf{Y}-axis$ lies in the same plane with a perpendicular direction and the $\mathbf{Z}-axis$ completes the direct reference frame.
The two star sensors located on the AVUM module are aligned with the following nominal orientation w.r.t the body reference frame, expressed trough Euler angles and quaternion rotations:

$$\begin{aligned} \alpha_{STR_{1_{nom}}} &= \begin{bmatrix} 150^\circ & 30^\circ & 0^\circ \end{bmatrix}' \\ q_{STR_{1_{nom}}} &= \begin{bmatrix} 0.2501 & -0.2500 & 0.0670 & 0.9330 \end{bmatrix}' \end{aligned} \tag{2.4}$$

$$\begin{aligned} \alpha_{STR_{1_{nom}}} &= \begin{bmatrix} 210^\circ & 30^\circ & 0^\circ \end{bmatrix}' \\ q_{STR_{1_{nom}}} &= \begin{bmatrix} -0.2271 & -0.2708 & 0.0146 & 0.9353 \end{bmatrix}' \end{aligned} \tag{2.5}$$

2.2 Attitude Parameterizations

There are several ways to parameterize attitude rotations: the most basic and applied is the attitude matrix which transforms a reference frame into another. Among the other widely used attitude parameterizations it's possible to include Euler angles, Euler parameters (also referred to as quaternions), Rodrigues parameters (or Gibbs vectors) and modified Rodrigues parameters.
In this section attitude modeling trough Euler angles and quaternions will be introduced.

2.2.1 Euler Angles

An Euler angles representation expresses a rotation from an initial frame I to a final frame F as the product of three successive rotations, with anti-clockwise direction considered as positive. The first rotation is about any axes, the second one is about either of the two axes still not used and the last is about either of the two not used for the second. There are 12 sets of Euler angles that describe all the possible combinations. The other 15, out of a total of 27 possible rotations, are performed with more than two consecutive rotations are made on the same axes [34].
Let F_1 be a first reference frame described by a set of unit vectors $(\hat{\mathbf{e}}_1, \hat{\mathbf{e}}_2, \hat{\mathbf{e}}_3)$ and F_2 a second reference frame, whose position with respect to the first one is described by another set of unit vectors $(\hat{\mathbf{E}}_1, \hat{\mathbf{E}}_2, \hat{\mathbf{E}}_3)$. Assume the position of the rigid body to be described, in each reference frame, by the tridimensional vectors:

$$\begin{aligned}\mathbf{v}_1 &= x\hat{\mathbf{e}}_1 + y\hat{\mathbf{e}}_1 + z\hat{\mathbf{e}}_1 \\ \mathbf{v}_2 &= X\hat{\mathbf{E}}_1 + Y\hat{\mathbf{E}}_1 + Z\hat{\mathbf{E}}_1\end{aligned} \tag{2.6}$$

It's possibile to use a coordinate transformation matrix $\mathbf{L}_{21}$, as function of the three rotation angles (ϕ, θ, ψ) and expressed in terms of three elementary rotation matrices, to switch from a reference to another:

$$\mathbf{v}_2 = \mathbf{L}_{21}\mathbf{v}_1 \tag{2.7}$$

Using this coordinate transformation formulation, it's possible to describe the attitude of the orbital frame w.r.t the ECI frame.
Multiple sequence exist to rotate these reference frame, *3-1-3*, *3-2-1* and *1-2-3* are the most used.
For example, considering the elementary rotations matrices for the sequence *3-1-3*, often used for analytical formulation of rigid body motion, typical of spinning spacecraft:

$$\mathbf{L}_{BI} = \mathbf{R}_3(\phi)\mathbf{R}_1(\theta)\mathbf{R}_3(\psi) \tag{2.8}$$

where

$$\mathbf{R}_3(\psi) = \begin{bmatrix} cos(\psi) & sin(\psi) & 0 \\ -sin(\psi) & cos(\psi) & 0 \\ 0 & 0 & 1 \end{bmatrix} \tag{2.9}$$

$$\mathbf{R}_1(\theta) = \begin{bmatrix} 1 & 0 & 0 \\ 0 & cos(\theta) & sin(\theta) \\ 0 & -sin(\theta) & cos(\theta) \end{bmatrix} \tag{2.10}$$

$$\mathbf{R}_3(\phi) = \begin{bmatrix} cos(\phi) & sin(\phi) & 0 \\ -sin(\phi) & cos(\phi) & 0 \\ 0 & 0 & 1 \end{bmatrix} \tag{2.11}$$

which summed up

$$L_{BI} = \begin{bmatrix} c(\phi)c(\psi) - s(\phi)c(\theta)s(\psi) & s(\phi)c(\theta)c(\psi) + c(\phi)s(\psi) & s(\phi)s(\theta) \\ -c(\phi)c(\theta)s(\psi) - s(\phi)c(\psi) & c(\phi)c(\theta)c(\psi) - s(\phi)s(\psi) & c(\phi)s(\theta) \\ s(\theta)s(\psi) & -s(\theta)c(\psi) & c(\theta) \end{bmatrix} \tag{2.12}$$

where in the aerospace and nautical field ϕ, θ, and ψ are known as *roll*, *pitch* and *yaw*, respectively. Or in a more strict aeronautical terminology: *bank*, *attitude* and *heading*.
As a result from the properties of orthogonal matrices, the inverse is equal to its transpose $\mathbf{L}_{21} = \mathbf{L}_{12}^T$ and can be thus easily calculated without invoking the matrix

inverse heavy operations.
For sake of completeness, the coordinate rotation matrix for the rotation sequence *3-2-1* is also reported

$$L_{BI} = \begin{bmatrix} c(\phi)c(\theta) & c(\phi)s(\theta)s(\psi) + s(\phi)c(\psi) & s(\phi)s(\psi) - c(\phi)s(\theta)c(\psi) \\ -s(\phi)c(\theta) & c(\phi)c(\psi) - s(\phi)s(\psi)s(\theta) & c(\phi)s(\psi) + s(\phi)s(\theta)c(\psi) \\ s(\theta) & -s(\psi)c(\theta) & c(\theta)c(\psi) \end{bmatrix} \tag{2.13}$$

where $c(\theta) = cos(\theta)$ and $s(\theta) = sin(\theta)$.
Finally the general rotation of α around the $Y - axis$ is modeled as:

$$\mathbf{R}_2(\alpha) = \begin{bmatrix} cos(\alpha) & 0 & -sin(\alpha) \\ 0 & 1 & 0 \\ sin(\alpha) & 0 & cos(\alpha) \end{bmatrix} \tag{2.14}$$

However, this parametrization holds singularities at pitch value of $\theta = \pi/2 + k\pi$. This singularity is known as *gimbal lock* and precludes Euler angles formulation adoption where high angles could be reached, as generally happens for space application. Common practice is to change reference system whenever the system state is reaching a singularity and thus avoiding divergence, but overall only standard atmospheric vehicles with a bounded flight envelope could be suited for Euler's angles attitude models.

2.2.2 Quaternions

Quaternions, also referred to as Euler parameters have been introduced by Euler and later William Rowan Hamilton in 1843 and applied in tridimensional mechanics as hyper-complex number[2] of rank 4 [34]. Unlike the Euler angles which represent a coordinate change by a series of rotations around the S/C body axes, quaternions represent it with just one rotation $\boldsymbol{\alpha}$ around a single axis $\hat{\mathbf{a}}$.

$$\mathbf{q} = q_0 + \mathbf{q}_{1:3} = q_0 + q_1\mathbf{i} + q_2\mathbf{j} + q_3\mathbf{k} \tag{2.15}$$

Quaternions are four-component vectors, composed by a scalar component q_0 which represents the magnitude of the rotation, and a three-component vector $\mathbf{q}_v$, a scaled form of the eigenvector, i.e. the rotation axis.

$$\begin{aligned} q_0 &= cos(\alpha/2) \\ q_1 &= a_1 cos(\alpha/2) \\ q_2 &= a_2 cos(\alpha/2) \\ q_3 &= a_3 cos(\alpha/2) \end{aligned} \tag{2.16}$$

[2]A hypercomplex value is a number having hybrid properties departing from those of the real and complex numbers

Moreover there is an important property regarding quaternions that guarantees the attitude matrix to be orthogonal:

$$\|\mathbf{q}\| = q_0^2 + q_1^2 + q_2^2 + q_3^2 = 1 \tag{2.17}$$

Quaternions also satisfy the constraint

$$\mathbf{q}\mathbf{q}^T = 1 \tag{2.18}$$

It is worthwhile to note that, by convention, q_0 is always nonnegative for $\alpha \in [-\pi, \pi]$.

In order to handle a quaternion formulation, two operations must be highlighted: quaternion inverse and quaternion product. The first is defined as follows:

$$\mathbf{q}^{-1} = \frac{\mathbf{q}^*}{\|\mathbf{q}\|_2} = \frac{[q_0, -q_1, -q_2, -q_3]^T}{q_0^2 + q_1^2 + q_2^2 + q_3^2} \tag{2.19}$$

where $\mathbf{q}^*$ is defined as the conjugate quaternion.
Quaternions product is expressed as

$$\mathbf{q} = \mathbf{q}' \otimes \bar{\mathbf{q}} \tag{2.20}$$

and it can be represented by matrix multiplication

$$\mathbf{q} = \boldsymbol{\Omega}(q')\bar{\mathbf{q}} = \boldsymbol{\Psi}(\bar{q})\mathbf{q}' \tag{2.21}$$

where

$$\boldsymbol{\Omega}(q') = \begin{bmatrix} q_0' & -\mathbf{q}_v'^T \\ \mathbf{q}_v' & q_0\mathbb{I}_3 + [\mathbf{q}_v\times] \end{bmatrix} \tag{2.22}$$

$$\boldsymbol{\Psi}(\bar{q}) = \begin{bmatrix} \bar{q}_0 & -\bar{\mathbf{q}}_v^T \\ \bar{\mathbf{q}}_v & \bar{q}_0\mathbb{I}_3 + [\bar{\mathbf{q}}_v\times] \end{bmatrix} \tag{2.23}$$

where $\mathbb{I}_3$ is 3×3 identity matrix and $[\mathbf{q}\times]$ is the skew-symmetric matrix defined as

$$[\mathbf{q}\times] = \begin{bmatrix} 0 & -q_3 & q_2 \\ q_3 & 0 & -q_1 \\ -q_2 & q_1 & 0 \end{bmatrix} \tag{2.24}$$

The latter identity can be also useful to compute cross product of two three-dimensional vectors as

$$\mathbf{x} \times \mathbf{y} = [\mathbf{x}\times]\mathbf{y} \tag{2.25}$$

$$[\mathbf{q}\otimes] \equiv \begin{bmatrix} q_0 & -\mathbf{q}_v^T \\ \mathbf{q}_v & q_0\mathbb{I}_3 - [\mathbf{q}_v\times] \end{bmatrix} = \begin{bmatrix} \mathbf{\Psi q} & \mathbf{q} \end{bmatrix} \tag{2.26}$$

and

$$[\mathbf{q}\odot] \equiv \begin{bmatrix} q_0 & -\mathbf{q}_v^T \\ \mathbf{q}_v & q_0\mathbb{I}_3 + [\mathbf{q}_v\times] \end{bmatrix} = \begin{bmatrix} \mathbf{\Xi q} & \mathbf{q} \end{bmatrix} \tag{2.27}$$

with $\mathbf{\Psi}(\mathbf{q})$ and $\mathbf{\Xi}(\mathbf{q})$ representing the 4×3 matrices

$$\mathbf{\Psi}(\mathbf{q}) \equiv \begin{bmatrix} -\mathbf{q}_v^T \\ q_0\mathbb{I}_3 - [\mathbf{q}_v\times] \end{bmatrix} = \begin{bmatrix} -q_1 & -q_2 & -q_3 \\ q_4 & q_3 & -q_2 \\ -q_3 & q_4 & q_1 \\ q_2 & -q_1 & q_4 \end{bmatrix} \tag{2.28}$$

$$\mathbf{\Xi}(\mathbf{q}) \equiv \begin{bmatrix} -\mathbf{q}_v^T \\ q_0\mathbb{I}_3 + [\mathbf{q}_v\times] \end{bmatrix} = \begin{bmatrix} -q_1 & -q_2 & -q_3 \\ q_4 & -q_3 & q_2 \\ q_3 & q_4 & -q_1 \\ -q_2 & q_1 & q_4 \end{bmatrix} \tag{2.29}$$

$$q \otimes p = \begin{bmatrix} q_0 \cdot p_0 - \mathbf{q}_v^T \cdot \mathbf{p}_v \\ p_0 \cdot \mathbf{q}_v + q_0 \cdot \mathbf{p}_v - \mathbf{q_v} \times \mathbf{p_v} \end{bmatrix} \tag{2.30}$$

The product of two quaternions is not commutative but the associative and distributive properties hold.
It's possible to define the coordinate transformation matrix trough a quaternion formulation as

$$\mathbf{L}_{BI} = (|q_0|^2 - \|\mathbf{q}_v\|^2)\mathbb{I}_3 + 2\mathbf{q}_v\mathbf{q}_v^T + 2q_0[\mathbf{q}_v\times] \tag{2.31}$$

or in a more extended form

$$\mathbf{L}_{BI} = \begin{bmatrix} q_0^2 + q_1^2 - q_2^2 - q_3^2 & 2q_1q_2 + 2q_0q_3 & 2q_1q_3 - 2q_0q_2 \\ 2q_1q_2 - 2q_0q_3 & q_0^2 - q_1^2 + q_2^2 - q_3^2 & 2q_2q_3 + 2q_0q_1 \\ 2q_1q_3 + 2q_0q_2 & 2q_2q_3 - 2q_0q_1 & q_0^2 - q_1^2 - q_2^2 + q_3^2 \end{bmatrix} \tag{2.32}$$

The largest part of spacecraft models for attitude determination and estimation are based either on a *Euler angles* or *quaternion* description. Euler angles' models have been proved to be very efficient as long as the model linearity holds. However they bring several drawbacks: the point around which the linearization is performed may not work along all the flight envelope, causing the the model to not reach global stability; the rotational sequences behind the Euler angle representation contain a singularity at high angles of attack, therefore its use is preferred in aeronautic where the angles are smaller to avoid gimbal-lock.

On the other hand, quaternion based models are much more robust. They do not hold non linearities or rely on rotational sequences and can globally stabilize the system. Furthermore, since no trigonometric relations exist in the quaternion kinematic differential equations and only products need to be calculated, they are well suited for onboard real-time computation [35]. Moreover quaternions results to perform better also in control algorithms, making them suitable for a wide range of attitude control application.
For these reasons a quaternion formulation has been implemented in this thesis.

2.3 Attitude Kinematics

The evolution of the quaternion components is described by a set of nonlinear differential equations, represented in matrix form as:

$$\frac{d}{dt}\mathbf{q}(t) = \frac{1}{2}\mathbf{\Omega}(\boldsymbol{\omega}_B(t))\mathbf{q}(t) \tag{2.33}$$

$$\begin{aligned}\begin{Bmatrix}\dot{q}_0\\ \dot{q}_1\\ \dot{q}_2\\ \dot{q}_3\end{Bmatrix} &= \frac{1}{2}\begin{bmatrix}0 & -\omega_1 & -\omega_2 & -\omega_3\\ \omega_1 & 0 & \omega_3 & -\omega_2\\ \omega_2 & -\omega_3 & 0 & \omega_1\\ \omega_3 & \omega_2 & -\omega_1 & 0\end{bmatrix}\begin{Bmatrix}q_0\\ q_1\\ q_2\\ q_3\end{Bmatrix}\\ &= \frac{1}{2}\begin{bmatrix}q_0 & -q_1 & -q_2 & -q_3\\ q_1 & q_0 & -q_3 & q_2\\ q_2 & q_3 & q_0 & -q_1\\ q_3 & -q_2 & q_1 & q_0\end{bmatrix}\begin{Bmatrix}0\\ \omega_1\\ \omega_2\\ \omega_3\end{Bmatrix}\end{aligned} \tag{2.34}$$

where $\mathbf{q} \in \mathbb{R}^4$ represent the current attitude quaternion solution.
A second formulation [36] can be implemented as a reduced model with a lower computational load and more suited to make the system controllable. In this case the vectorial part is the only one implemented while the scalar element is embedded in the unit length constraint. This formulation also prevent to occur in the singularity hidden in full quaternion model covariance matrix [9].

Splitting quaternion propagation in its scalar and vectorial part, spacecraft kinematics can be rewritten as:

$$\begin{aligned}\dot{q}_0 &= -\frac{1}{2}\boldsymbol{\omega}_B^T \cdot \mathbf{q}\\ \dot{\mathbf{q}} &= -\frac{1}{2}\boldsymbol{\omega}_B \times \mathbf{q} + \frac{1}{2}q_0\boldsymbol{\omega}_B\end{aligned} \tag{2.35}$$

or in a more compact formulation as:

$$\dot{\mathbf{q}}(t) = \frac{1}{2}\begin{bmatrix} 0 & -\boldsymbol{\omega}_B^T \\ \boldsymbol{\omega}_B & -[\boldsymbol{\omega}_B \times] \end{bmatrix}\mathbf{q}(t) \tag{2.36}$$

Equation 2.36 is then numerically integrated using the onboard flight computer to determine the spacecraft orientation. Angular rates are evaluated by gyros in a *strapdown inertial reference system*[3].

2.4 Rigid-Body Attitude Dynamics

Let $\mathbf{J} \in \mathbb{R}^3$ be the inertia matrix of a spacecraft and expressed by the inertia tensor in body axes as:

$$\mathbf{J} = \begin{bmatrix} J_{11} & J_{12} & J_{13} \\ J_{21} & J_{22} & J_{23} \\ J_{31} & J_{32} & J_{33} \end{bmatrix} \tag{2.37}$$

If the S/C body axes are aligned with the principal axes frame, the inertia matrix becomes diagonal. Moreover if the body features some symmetries in the mass distribution they will reflect in the inertia matrix terms components. Uncertainties regarding the inertia matrix could also introduce some noise the simulation process.

Ignoring the effects of structural flexibility and liquid sloshing, the angular momentum for a rigid body is described as follows:

$$\mathbf{H}_I = \mathbf{J}\boldsymbol{\omega}_I \tag{2.38}$$

where $\boldsymbol{\omega}_I \in \mathbb{R}^3$ represent the angular velocity vector w.r.t an inertial frame. Considering the inertial and body frame, the general dynamic equation of rigid body rotation as a function of all the torques acting on the system can be written as:

$$\frac{d}{dt}\mathbf{H} = \Sigma\mathbf{T} \tag{2.39}$$

In order to study orbital motion for a nadir pointing spacecraft it's convenient to express the angular velocity of the body frame relative to the LVLH frame. Since the local frame x and z axes are aligned with the orbital velocity vector and Nadir direction, they remain in the orbital plane. While x and z direction vary along the

[3]In a strapdown reference system the inertial sensors are mounted rigidly on the structure. Therefore output are expressed directly in body frame.

orbit, y is invariant.
Therefore the angular velocity of the local frame is:

$$\boldsymbol{\omega}_{LVLH} = \begin{Bmatrix} 0 \\ -\omega_0 \\ 0 \end{Bmatrix} \tag{2.40}$$

where ω_0 represents the orbital mean motion and the minus sign results from the right hand rule.
Considering $\boldsymbol{\omega}_B$ as the body rate w.r.t the LVLH frame represented in body frame and $\boldsymbol{\omega}_{LVLH}$ the orbital velocity with respect to the inertial frame, represented in LVLH frame, then:

$$\boldsymbol{\omega}_I = \boldsymbol{\omega}_B + \mathbf{L}_{BI} \cdot \boldsymbol{\omega}_{LVLH} \tag{2.41}$$

Introducing the input torques $\mathbf{T}$ in the system and considering the inertia matrix time invariant, the Euler's equation is obtained:

$$\dot{\omega}_I = \mathbf{J}^{-1}[-\boldsymbol{\omega}_I \times (\mathbf{J} \cdot \boldsymbol{\omega}_I + \mathbf{H}_{rws}) + \mathbf{T}_b - \mathbf{T}_{cont}] \tag{2.42}$$

where $\mathbf{H}_{rws}$ is the total angular momentum if reaction wheels are used, $\mathbf{T}_b$ includes all the external torques and $\mathbf{T}_{cont}$ represents the control torque delivered by the acutation system. All the resulting torques are resolved in body frame. In the latter equation the cross product between $\boldsymbol{\omega}_B$ and $\mathbf{H}_{rw}$ represent the satellite and RWS gyroscopic coupling.
For this thesis work's purposes, reaction system has not been modeled in the simulation environment, thus its angular momentum is discarded. Then from Eq.2.42:

$$\begin{aligned}
\dot{\omega}_1 &= \frac{(J_2 - J_3)}{J_1}\omega_2\omega_3 + \frac{1}{J_1}T_1 \\
\dot{\omega}_2 &= \frac{(J_3 - J_1)}{J_2}\omega_1\omega_3 + \frac{1}{J_2}T_2 \\
\dot{\omega}_3 &= \frac{(J_1 - J_2)}{J_3}\omega_1\omega_2 + \frac{1}{J_3}T_3
\end{aligned} \tag{2.43}$$

The differential equation in Eq.2.43 can be integrated to determine the time history of the angular velocity components as a function of the applied torque, both external and internal. In turn, these can be used to obtain the attitude evolution, in terms of quaternions or Euler's angles.

In a first analysis approach, the assumption of rigid body for the study of the attitude of a satellite is acceptable but it can easily fail in presence of large deployable structure, i.e. solar arrays. Moreover external and internal disturbances, such as thrusters firing, internal rotating components and liquid sloshing could cause vibrations of the structure around its natural frequencies and reduce the rigid body assumption accuracy.

2.5 Torques

Generally, the torques acting on a space vehicle can be divided in internal and external torques. Internal couples can be generated by the attitude control systems, the on-board equipment motion and liquids sloshing in the tanks. Instead, the external are mainly disturbance torques function of the environment in which the S/C operates. Both need to be accurately modeled in order to comply with mission pointing requirements and achieve spacecraft control.
The overall torque acting on the S/C can be thus expressed as

$$\mathbf{T} = \mathbf{T}_{ext} + \mathbf{T}_{int} \tag{2.44}$$

Several disturbance sources act on the S/C, with their magnitude strongly depending from mission parameters, in particular from altitude and orbit inclination. The most relevant disturbance torques are: *gravity gradient torque, atmospheric drag torque, solar radiation torque and magnetic dipole torque*, with other sources whose torques values lie below $10^{-5}Nm$

$$\mathbf{T} = \mathbf{T}_{gg} + \mathbf{T}_{drag} + \mathbf{T}_{solar} + \mathbf{T}_{mag} \tag{2.45}$$

Among these disturbances, gravity gradient torque is the only one to be wholly deterministic and to have an analytical closed form solution, assigned S/C altitude and attitude; the other three disturbance torques are stochastic variables and can't be predicted with the same accuracy.

As previously mentioned, internal torques are couples that build up internally the S/C either by moving parts, control systems, flexible booms or solar panels, liquid sloshing inside the tanks and even astronauts if we are considering a manned spacecraft. Spacecraft themselves are constituted by multiple more or less rigid bodies connected by joints, resulting in a high number of degrees of freedom. Internal torques must be accounted in order to predict the S/C attitude propagation, because the system kinetic energy can be redistributed with non negligible amount. For S/C with large deployable booms or solar arrays an internal torques and flexibility analysis could be essential for mission success.

In the following pages these disturbance are modeled in the body frame, with the analytic demonstrations referred in [37] and [38].

2.5.1 Control Torque

Every space mission requires a certain type of attitude control, either to execute orbit maneuvers or guarantee precision pointing during science, communication or surveillance activities.
Several actuation systems exist to provide three-axis control for space vehicle and their selection strictly depends on mission parameters and constraints. For example spinning stabilized and three-axis stabilized satellites feature a different suite of sensors and actuators. Some of the most mature technologies include: reaction wheels, control moment gyros, magnetic coils, hot and cold gas thrusters.

Reaction wheel are essentially torque generators with high inertia rotors which provide smooth control allowing for precision pointing. Angular momentum conservation causes the wheel to be accelerated in one direction and generate an opposite reaction torque. Drawbacks include vibrations, jitter[4] and angular moment accumulation that needs to be discharged by mean of some actuator ignition (such as thrusters).
In order to achieve a complete three-axis control, at least three wheels with non-coplanar spin axis are required. Usually at least another wheel is inserted for redundancy and reliability purposes.

Control moment gyro (CMG) are basically reaction wheels with a nominal non-zero spin rate providing a nearly constant angular momentum and momentum bias stiffness, also referred to as gyroscopic stability. They are similar to the momentum wheels, except for the wheel spin-axis to be gimbaled. This property leads the CMG to be a torque amplifier and thus suited for spacecraft needing large controlling torques. In the actuator system selection the principal driving parameters are torque level saturation and angular momentum capacity.

Magnetic Torquers are crafty control actuators that exploit the Earth's magnetic field in order to produce momentum. Magnetic torquers are generally wire coils distributed along the spacecraft that, housing flux of electrical current, generate a magnetic dipole. However this torque can only be delivered along the perpendicular axis to the instantaneous Earth's magnetic field vector direction. Moreover spacecraft placed in orbit with low inclinations can't be equipped with this kind of systems since there is not much variation of magnetic field in the equatorial regions and thus it will provide really weak torques.

Thrusters are among the most used equipment since they also provide correction of orbital parameters and angular moment desaturation. If a spacecraft

[4]Jitter refers to un-commanded high frequency motions above the S/C control bandwidth

is equipped with multiple thrusters, the ignition of some of them can rotate the vehicle in the desired direction. Extending this argument, in order to acquire a complete three axis control a minimum of six thruster are needed. Hot gas thruster are fed with propellent to be ignited and thermodynamically expanded trough nozzle. Generally monopropellant systems with hydrazine and hypergolic mixtures[5] are used since only one tank and no ignitor are required. Instead, cold gas thrusted do not need to be altered chemically and provide torques by fuels state change or high pressure storage.

Besides the actuation system, both a guidance system and a controller are required to define a certain error and produce the correct torque in the commanded direction. For the simulation, the desired attitude is assumed to be the unity quaternion

$$\mathbf{q}_{ref} = \begin{bmatrix} 1 \\ 0 \\ 0 \\ 0 \end{bmatrix} \tag{2.46}$$

meaning the body axes are aligned with the LVLH reference frame's axes.
A guidance system and feedback controller have been implemented to compute the attitude and attitude rate error, defined as the difference between the actual and desired attitude and evaluate the control torques required. For application where the spacecraft's body rates are bounded to small values, the three-axis control system can be decoupled into three independent motions, without loss of accuracy.

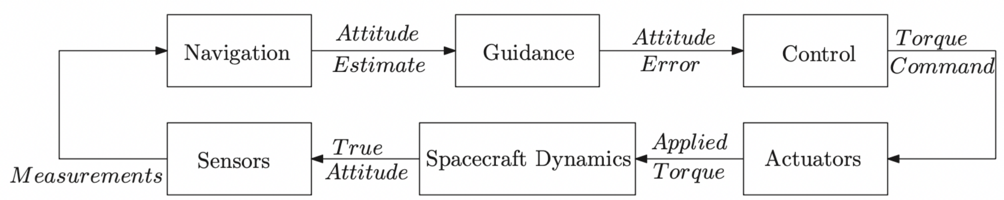

Figure 2.5: Satellite attitude control loop [37]

The control law is a simple PD controller that receives attitude and angular rate error and drives them to zero [35]

$$\mathbf{T}_{contr} = -K_p \cdot \mathbf{q}_{v_{err}} \cdot sign(q_{0_{err}}) - K_d \cdot \boldsymbol{\omega}_B \tag{2.47}$$

[5]Hypergolic fuels ignite without sparks by just coming in contact and thus enables to get rid of the ignition system.

where $\mathbf{q}_{err}$ is quaternion error w.r.t the desired attitude, composed by a scalar and vectorial error $q_{0_{err}}$ *and* $\mathbf{q}_{v_{err}}$, $\boldsymbol{\omega}_B$ is the angular velocity error and K_p and K_d are the *proportional* and *derivative gains*. If both gains are positive, the motion results to be stable.
In particular the proportional gain defines the magnitude of control torque computed linearly from the state error and the steady state error. Moreover the value of K_p also sets the control system's bandwidth[6].
The derivative gain K_d directly affects the stability of the system reducing the damping. Generally, increasing the value of K_d slows down the system response but improves stability margins.
If the steady state error is larger than the maximum allowable value, an integrator gain K_i should be added. However this term tends to reduce the stability margins. It results that control system's desired performance can be achieved only after an appropriate gain tuning.

While the angular rate error is simply calculated as a difference between the actual and desired angular velocity, i.e. zero, to achieve stability, quaternion error is not a simple difference but it must be computed using quaternion's product rules, between the desired quaternion's inverse, as defined in Eq.2.19, and the actual S/C attitude quaternion:

$$\mathbf{q}_{err} = \mathbf{q}_{des}^{-1} \otimes \mathbf{q}_{true} \tag{2.48}$$

$$\mathbf{q}_{des} = \mathbf{q}_{des}^{-1} = \frac{\mathbf{q}_{des}^{*}}{||\mathbf{q}_{des}||_2} = \frac{[q_0 - q_1 - q_2 - q_3]^T}{q_0^2 + q_1^2 + q_2^2 + q_3^2} \tag{2.49}$$

where $\mathbf{q}_{true}$ represent the instantaneous quaternion from the integration of S/C dynamic equations.
Quaternion error results to be:

$$\mathbf{q}_{err} = \mathbf{q}_{des} \otimes \mathbf{q}_{true} = \begin{bmatrix} q_{0_{err}} \\ q_{1_{err}} \\ q_{2_{err}} \\ q_{3_{err}} \end{bmatrix} = \begin{bmatrix} q_{0_{des}} & -q_{1_{des}} & -q_{2_{des}} & -q_{3_{des}} \\ q_{1_{des}} & q_{0_{des}} & -q_{3_{des}} & q_{2_{des}} \\ q_{2_{des}} & q_{3_{des}} & q_{0_{des}} & -q_{1_{des}} \\ q_{3_{des}} & -q_{2_{des}} & q_{1_{des}} & q_{0_{des}} \end{bmatrix} \cdot \begin{Bmatrix} q_{0_{true}} \\ q_{1_{true}} \\ q_{2_{true}} \\ q_{3_{true}} \end{Bmatrix} \tag{2.50}$$

It should be pointed out that feedback control quality depends on the measurement data reliability. In an ideal case, i.d. error-free measurements, the controller receives the real state and reaches stability in a lower time frame. But in reality,

[6]The bandwidth defines the range of frequency a particular system can handle, the higher it is the more accurate the control can be.

measurements data come with errors, so the controller should be fed with the estimated states.

Assuming that satellite motion is sufficiently slow and the control torques are strong compared to the disturbances, it is possible to consider Euler dynamics decoupled about the three rigid body principal axes.
The PD controller gives as output a three dimensional torque:

$$\mathbf{T}_{contr} = \begin{bmatrix} T_x \\ T_y \\ T_z \end{bmatrix} \tag{2.51}$$

the control torque vector will be implemented in Eq.2.42 to evaluate the dynamic response of the spacecraft.

2.5.2 Gravity Gradient Torque

The motion of a rigid body in a gravitational field is described by Newton's laws where each point in space is to be subjected to different values of gravitational force. Generally it can be written as:

$$\mathbf{F_g} = \frac{GMm\mathbf{r_b}}{|\mathbf{r}|^3} \tag{2.52}$$

where G has been introduced in Eq.2.3, $\mathbf{r}_b$ is the distance between the Earth's center and the S/C center of mass. M and m are the mass of planet and of S/C, respectively.

Gravity gradient torque arises when the vehicle structure is large enough to experience a non-uniform force field. This difference results in a couple acting on any satellite with a non symmetrical mass distribution along the Nadir direction and whose magnitude is a relevant component in the space environment.
The planet's gravitational force acting on the S/C can be formulated assuming a spherical mass distribution for the orbiting planet, in this case the Earth, with good approximation for a wide range of applications.
In order to obtain the expression for the gravity torque on a continuous body, the gravitational force on a mass element is firstly computed and then integrated to get the total torque about the center of mass. The resulting formulation is:

$$\mathbf{T}_{gg} = \frac{3\mu}{\mathbf{r}_b^3}[\mathbf{r}_b \times (\mathbf{J}\mathbf{r}_b)] \tag{2.53}$$

Since the gravity gradient torque needs to be represented in the body frame and noticing that in the LVLH frame the Earth to spacecraft vector is defined as:

$$\mathbf{R} = \begin{bmatrix} 0 \\ 0 \\ -|\mathbf{R}| \end{bmatrix} \tag{2.54}$$

Letting $\mathbf{q}$ be the quaternion transformation between the body frame and LVLH frame, using Eq.2.32:

$$\mathbf{R} = \begin{bmatrix} q_0^2+q_1^2-q_2^2-q_3^2 & 2q_1q_2+2q_0q_3 & 2q_1q_3-2q_0q_2 \\ 2q_1q_2-2q_0q_3 & q_0^2-q_1^2+q_2^2-q_3^2 & 2q_2q_3+2q_0q_1 \\ 2q_1q_3+2q_0q_2 & 2q_2q_3-2q_0q_1 & q_0^2-q_1^2-q_2^2+q_3^2 \end{bmatrix} \begin{bmatrix} 0 \\ 0 \\ -|\mathbf{R}| \end{bmatrix} \tag{2.55}$$

This torque can be expressed in the dyadic form by extracting the last column of the DCM matrix ($\mathbf{R}_3$):

$$\mathbf{T}_{gg} = 3\boldsymbol{\omega}^2_{LVLH}(\mathbf{R}_3 \times \mathbf{J}\mathbf{R}_3) \tag{2.56}$$

In the latter formulation the difference between the spacecraft geometric center and its center of mass has been discarded, or more precisely assumed to be 1 m. Moreover a few characteristics can be deduced: the torque results to be both normal to the local vertical and inversely proportional to the cube of the geocentric distance. It's clear that for a symmetrical S/C, this disturbance vanishes.

For low Earth orbits, this is normally among the biggest disturbance acting on the S/C and its magnitude strongly depends on the S/C structure form and orientation in space. For example boom equipped spacecrafts are subject more than other to this kind of torque.
However, the knowledge and predictability of this disturbance can be used as an effective source for S/C passive attitude control and stabilization.

2.5.3 Atmospheric Drag Torque

This disturbance torque is relevant only for low Earth orbits where some residual atmosphere is present. As a matter of fact, for satellite orbiting below 400 km, aerodynamic drag is the dominant external torque. However, at this height, density level is so low that a continuous model is no more effective and so the atmosphere and spacecraft interactions need to be treated at molecular level.
CIRA-2012 [39](*the Committee on Space Research - COSPAR - International Reference Atmosphere 2012*) defines the structure of the Earth's upper atmosphere (above 120 km) and provides accepted empirical model to describe its thermodynamical properties in LEO.

Considering a Space Rider nominal orbit altitude of 400 km, with a moderate solar and geomagnetic activity, the atmosphere density results to be:

$$\rho = 3.96 \cdot 10^{-12} \frac{kg}{m^3} \tag{2.57}$$

Since this topic lies beyond the scope of this thesis, a few assumption are considered and a simple drag model is developed. The phenomenon is modeled as an elastic impact without reflection, meaning that the molecule sticks to the vehicle and their momentum is totally lost. Moreover the S/C is considered not spinning and the thermal motion of the atmosphere is assumed to be smaller than the S/C orbital speed.
Aerodynamic drag torque can be thus formulated as:

$$\mathbf{T}_{drag} = \frac{1}{2}\rho C_d A_s \mathbf{V}^2 (c_{pa} - c_g) \tag{2.58}$$

where ρ is the atmospheric density in kg/m^3, C_d is the drag coefficient, A_s is the cross section area normal to the velocity vector, $\mathbf{V}$ is the satellite orbital velocity and $(c_{pa} - c_g)$ is the distance between the aerodynamic pressure center and mass center of the spacecraft, assumed to be unitary.

In order to exactly compute the aerodynamic drag exerting on the vehicle, shadowing of one or more part of the S/C should be considered since the magnitude of this disturbance could drastically change. Moreover the cross section area in many cases is inaccurate at modeling the exposed area, thus a variable effective area should be considered.
Several studies have been conducted to provide more accurate formulas to compute this torque but the most influencing therm remains the atmospheric density, really difficult to predict. In literature [40], six main elements have been addressed to as the source of density variation:

- solar activity
- geomagnetic activity
- diurnal variation
- annual variation
- seasonal-latitude variation of the lower thermo-sphere and helium-sphere
- rapid density fluctuations probability associated with tidal and gravity waves

2.5.4 Solar Radiation Torque

Radiation pressure impacting on the vehicle in form of electromagnetic waves results in a torque around the S/C center of mass. Since sunlight travels with massive particles, it has momentum and therefore it exerts pressure when illuminating an object. In space there are multiple sources of radiation acting on a LEO satellite,

such as solar illumination, planet's albedo[7] and atmosphere reflection.
Besides the difficulty to calculate the effective radiative pressure on a multi-material, complex geometry body, solar radiation is also really tricky to predict since it's constantly varying as function of multiple parameters. A few examples are vehicle's position along the orbit, solar flare activity, exposed surface geometry, structure materials and angle of incidence. Moreover each S/C orientation implies a different illuminating condition, with more than one type of material exposed to sunlight.
For these reasons and because orbital motion has not been implemented, solar radiation torque is formulated in the worst case possible, to account for the highest disturbance.
A good estimate of this disturbance is given by [38]:

$$\mathbf{T}_{solar} = \mathbf{p}A_s(1 + r_f)cos(\phi)(c_{pa} - c_g) \tag{2.59}$$

where r_f is the reflectance factor, ranging from 0 for perfect absorption and 1 for perfect reflection (in this case assumed equal to 0.6). And $\mathbf{p}$ is the effective pressure on spacecraft surfaces, computable with the solar constant value at this altitude $F_s = 1.366W/m^2(at\ 1\ AU$[8]$)$ and the speed of light $c = 3 \cdot 10^8 m/s$

$$\mathbf{p} = \frac{F_s}{c} = 4.56 \times 10^{-6} N/m^2 \tag{2.60}$$

Lastly, A_s is the effective sunlit S/C area. Having considered that Space Rider is mostly an Earth pointing spacecraft, this area should be limited. For the simulation this torque has been implemented assuming a uniform reflectance and a null solar incidence angle ($\phi = 0°$).

2.5.5 Magnetic Dipole Torque

Magnetic disturbance torques results from the interaction between the planet's geomagnetic field, if present, and the S/C residual magnetic field, mainly generated by the electrical on-board equipments.
The Earth's liquid core generates a magnetic field that has important effects on the surrounding environment and results in a magnetic torque if the direction of the S/C residual dipole is not aligned with the local magnetic field.
In a first analysis the magnitude of this torque can be formulated as:

$$\mathbf{T}_{mag} = \mathbf{D} \cdot \mathbf{B} = \frac{2\mathbf{DM}}{R^3}\lambda \tag{2.61}$$

[7] Albedo refers to the reflection of the solar light from a planet, which, for a LEO spacecraft, is mostly constituted by Earth and Moon albedo.

[8] The Astronomical Unit is a fixed distance that indicates the Earth's mean distance from the Sun

where **D** is the S/C residual dipole: spacecraft residual moment ranges anywhere from 0.1 *to* 20 Am^2 [38], as a function of the on-board equipments and materials. **B** is the Earth magnetic field in *Tesla*. The latter can be calculated from the Earth's magnetic moment multiplied by the magnetic constant $\mathbf{M} = 7.96 \cdot 10^{15} kg/m$, **R** is the distance between the S/C and the Earth's center in m and λ is a function of the magnetic latitude that ranges from 1 at the magnetic equator and 2 to the magnetic poles.
It results that a S/C on a polar orbit will experience this disturbance twice stronger to the maximum it would in an equatorial orbit.
Likewise the gravity gradient, the *magnetic dipole torque* is usually exploited for passive control the S/C attitude by means of magnetic torque rods or other magnetic devices.

Chapter 3

Filtering for Attitude Estimation and Calibration

Attitude estimation is composed by two main processes: estimation of the vehicle's orientation w.r.t an appropriate reference system and filtering out the noisy measurements. The filtering process can be performed in several ways, such as using a combination of kinematic model propagated with three-axis rate integrating gyros or trough a dynamical model for the angular rate.
Accurate knowledge of real time spacecraft dynamics is a key aspect in order to provide a valid attitude solution. Sensors data is usually corrupted by several sources of noise, unknown disturbances or model uncertainties. Moreover the mass and volume constraints for space missions could likely drive towards spacecraft configurations without unnecessary and heavy sensors, with estimators and observers to provide state estimations.

While attitude deterministic methods always provide a solution, even if initialized with a really raw a priori dataset, estimation methods are more prone to diverge but could likely provide statistically optimal solutions, also with the possibility of tracking different parameters in the state vector. As a matter of fact attitude determination and estimation are used in a complementary fashion to enhance the performances of attitude determination systems.
In state estimation methods, there are two techniques to update the state vector: sequentially or recursively. In sequential estimators, the state vector is updated after each observation sampling. Instead, recursive estimators, also referred to as batch estimators, update the state vector using a series of past estimations, where the measurements experience partial derivation and are combined in a single updated state vector. The two major types of sequential estimators are recursive least-squares estimator and Kalman filter. Sequential estimators generally converge faster than batch processor but show less stability.

A meaningful state estimator provides solutions that will converge, in some sense, to the real states. In general this convergence means the difference between the estimated and actual state are bounded within the required limits, in order to guarantee, for example, compliance with pointing requirements. Recursive state estimators are also employed when the system measurements data are somehow interrupted or compromised.

For a general description of spacecraft state dynamics and outputs, the following representation is adopted:

$$\begin{aligned} \dot{\mathbf{x}}(t) =& f(\mathbf{x}(t), \mathbf{u}(t), t) + \mathbf{w}(t) \\ \mathbf{y}(t) =& h(\mathbf{x}(t)) + \mathbf{v}(t) \end{aligned} \tag{3.1}$$

where $f(\mathbf{x}(t), \mathbf{u}(t), t) \in \mathbf{R}^n$ represents the nonlinear dynamic equations and $h(\mathbf{x}(t), t) \in \mathbf{R}^m$ is the nonlinear measurement model.
The state vector includes all the attitude key variables, from the general attitude parameters to sensor biases and misalignments. The observation vector includes the output data of the on-board attitude sensors, raw or preprocessed in some useful format. Process noise, parameter uncertainties and unknown disturbances are embedded in $f(\mathbf{x}(t), \mathbf{u}(t), t)$ or lumped in $\mathbf{w}(t) \in \mathbf{R}^m$. The measurement vector $\mathbf{y} \in \mathbf{R}^m$ is corrupted by Gaussian white noise $\mathbf{v}(t)$. The vector $\mathbf{u}(\mathbf{t}) \in \mathbf{R}^p$ contains the known inputs. The superscript n, m and p, respectively, define the number of states, outputs and inputs.

Considered the time-invariant system as in Eq.3.1, when linearized it can be reformulated trough a set of matrices

$$\begin{aligned} \dot{\mathbf{x}}(t) =& A(t)\mathbf{x}(t) + B(t)\mathbf{u}(t) + \mathbf{w}(t) \\ \mathbf{y}(t) =& C(t)\mathbf{x}(t) + \mathbf{v}(t) \end{aligned} \tag{3.2}$$

where **A** and **B** are the states matrices, while **C** is the matrix relating the inputs to the outputs. The Linear Time-Invariant (LTI) system in Eq.3.2 holds as long as the nonlinearities are minimal.

3.1 Linearized state model

In this section is derived the quaternion based model for a Nadir pointing spacecraft with momentum wheel. The attitude is described by the rotations of the spacecraft body frame relative to the LVLH frame.
The system state is implemented using a state-space formulation with quaternion and angular body rate, stored into a 7×1 vector.

$$\mathbf{x}^T = \begin{bmatrix} \mathbf{q}^T \\ \boldsymbol{\omega}_B^T \end{bmatrix} \tag{3.3}$$

where attitude rate and quaternions are solutions of Eq.2.42 and Eq.2.35, respectively.
In order to deal with the nonlinear satellite equations, a linearization around steady state conditions must be carried out, without involving noises in the process.
Let $\Delta x(t)$ be the state-error vector, defined as the difference between the true and estimated state:

$$\Delta x(t) = x(t) - \hat{x}(t) = \begin{bmatrix} q - \hat{q} \\ \omega_B - \hat{\omega}_B \end{bmatrix} \tag{3.4}$$

The state perturbation equation is then derived trough the estimate solution

$$\Delta x(t) = f(x(t), t) - f(\hat{x}(t), t) + w(t) \tag{3.5}$$

Substituting into state perturbing equation:

$$\Delta x(t) = F(t)\Delta x(t) + w(t) \tag{3.6}$$

where $\mathbf{F}(t)$ is the 7x7 state transition matrix defined from Eq.2.22, Eq.2.29 and Euler's equation:

$$\mathbf{F(t)} = \begin{bmatrix} \frac{1}{2}\boldsymbol{\Omega}(\hat{\boldsymbol{\omega}}) & \frac{1}{2}\boldsymbol{\Xi}(\hat{\mathbf{q}}) \\ \mathbf{0}_{3x4} & \mathbf{J}^{-1}([\mathbf{J}\hat{\boldsymbol{\omega}}\times] - [\hat{\boldsymbol{\omega}}\times]\mathbf{J}) \end{bmatrix} \tag{3.7}$$

3.2 Linear Observers

Considering the LTI system described in Eq.3.2, a linear observer of all the states embedded in the state vector can be formulated as follows:

$$\begin{gathered} \dot{\hat{\mathbf{x}}} = A\hat{\mathbf{x}} + B\mathbf{u} + L(\mathbf{y} - C\hat{\mathbf{x}}) \\ \hat{\mathbf{y}} = C\hat{\mathbf{x}} \end{gathered} \tag{3.8}$$

where $\hat{\mathbf{x}}$ is the estimated state vector and $\mathbf{L} \in \mathbf{R}^{nxm}$ is the Luenberger gain, implemented to drive an error signal to zero. In case of linear observers, the error signal is defined trough the estimated output as $\tilde{\mathbf{y}} = \mathbf{y} - \hat{\mathbf{y}}$.
The observer's error dynamic is given by:

$$\begin{aligned} \dot{\mathbf{e}}(t) &= \dot{x} - \dot{\hat{x}} = A\mathbf{x} + B\mathbf{u} - [A\hat{\mathbf{x}} + B\mathbf{u} + L(\mathbf{y} - \hat{\mathbf{y}})] \\ \dot{\mathbf{e}}(t) &= A\mathbf{x} + B\mathbf{u} - [A\hat{\mathbf{x}} + B\mathbf{u} + L(C\mathbf{x} - C\hat{\mathbf{x}})] \\ \dot{\mathbf{e}}(t) &= (A - LC)(\mathbf{x} - \hat{\mathbf{x}}) = (A - LC)\mathbf{e} \end{aligned} \tag{3.9}$$

Thus the observer's error results to be a linear system whose dynamic is defined by:

$$\mathbf{e}(t) = \mathbf{e}^{(A-LC)t}\mathbf{e}(0) \tag{3.10}$$

In order to guarantee the error convergence to zero, independently from the initial condition, the eigenvalues of $(A-LC)$ must have a negative real component. This property is also referred to as *observability* of the system and can be also formulated trough matrix ranks as follows:

$$rank = \begin{bmatrix} C \\ CA \\ CA^2 \\ . \\ . \\ . \\ CA^{n-1} \end{bmatrix} = n \tag{3.11}$$

where n is the state vector's dimension.
The selection of the Luenberger gain should be carried out in a trade-off between fast error decay and effects of measurement noise on the system. The two behaviors depend on the real eigenvalues' absolute position. The more it is distant from the imaginary axis, the faster the error will converge to zero. Ideally, there are no limits on the gains' value since there is no physical system to be triggered, like for closed loop controls. Measurements' noise results to be the only limiting factor to set the gain arbitrarily high and obtain a really fast observer's response.
The only way to deal with this noise is to characterize it as a stochastic process and obtain optimal measurement recursively, like Kalman filters does. Moreover linear observers like Luenberger's could be unable to drive the error to zero in finite time in presence of model's uncertainties or unknown signals. For these reasons observers based in the sliding mode and Kalman filters are evaluated to provide robust attitude estimation.

3.3 Kalman Filter

Kalman filters are one of the most powerful tools for online estimation problems. The filter operates as a recursive mean squared error minimizer, estimating the dynamic state and filtering the noise.
Given a dynamical model of the system, KF minimizes the trace of the estimate error covariance, in a least squares sense, in order to obtain the most accurate estimate possible of the system state using a linear estimator based on present and past measurements. Since the loss function to be minimized is based indeed on

the mean square error, KF behaves like an optimal estimator for linear systems. Because Kalman filters combine data from multiple sensors, with different sampling frequency, they are also referred to as sensor fusion algorithms. They are suitable for both ground-based and on-board attitude determination but the effectiveness relies both on the dynamical model's accuracy and on the assumption that measurements' and process' noises are characterized by a Gaussian distribution with known standard deviation. The statistical distribution is used to build the covariance matrices related to the measurement and process noises, respectively $\mathbf{R}$ and $\mathbf{Q}$, from which is possible to evaluate the Kalman gain at each step.

3.3.1 Linear Kalman Filter

This section introduces the standard KF algorithms for continuous systems with discrete measurements. For a complete derivation of the filter reference is reported [41].

Consider the following linear stochastic dynamical system model from Eq.3.2:

$$\dot{x}(t) = A(t)\mathbf{x}(t) + G(t)\mathbf{w}(t) \tag{3.12}$$

with certain initial conditions and affected by some process white noise with zero mean and intensity:

$$\begin{gathered} E[w(t)] = 0 \\ E[w(t)w(t)^T(\tau)] = Q(t)\delta(t-\tau) \end{gathered} \tag{3.13}$$

As a matter of fact, sensors provide discrete measurements of the current state vector, from Eq.3.2:

$$\mathbf{y}_k = C_k\mathbf{x}(t_k) + \mathbf{v}_k \tag{3.14}$$

here v_k is a discrete white noise vector with zero mean and covariance[1] R_k, independent and uncorrelated from the process noise:

$$\begin{gathered} E[v_k] = 0 \\ E[v_k v_j^T] = R_k\delta_{kj} \end{gathered} \tag{3.15}$$

The choice of Q and R is driven by the available informations on the white noise distributions. Typically they are chosen as diagonal matrices with the noises' variances on the diagonal.
The goal in the design of a Kalman filter is to estimate the true model state subjected to process noise and filtering the noisy measurements $\mathbf{y}_k$, where $\mathbf{Q}$ and $\mathbf{R}_k$

[1] Covariance is defined as the tendency of two variables to simultaneously assume values higher or lower of their respective means.

are positive definite matrices.

The optimal solution of KF is based on the estimation error defined as:

$$\tilde{\mathbf{x}}(t) = \mathbf{x}(t) - \hat{\mathbf{x}}(t) \tag{3.16}$$

Indicating $P(t)$ as the error covariance matrix, assuming ($E[\tilde{\mathbf{x}}(t)] = 0$):

$$P(t) = E[\tilde{x}(t)\tilde{x}^T(t)] = E[(x - \hat{x})(x - \hat{x})^T] \tag{3.17}$$

Kalman filter's estimates are provided minimizing the trace of the error covariance matrix, i.e. minimizing the sum of the system state error variances, in terms of mean squared error.
Initially KF performs a state prediction, given the initial conditions of the state vector and the state covariance matrix, assuming noise-free system dynamics. State propagation is in form of differential equation as follows:

$$\begin{aligned} \dot{\hat{x}}(t) &= A(t)\hat{x}(t) \\ \dot{P}(t) &= A(t)P(t) + P(t)A^T(t) + G(t)Q(t)G(t) \end{aligned} \tag{3.18}$$

Between each measurement, state estimation propagates according to Eq.3.18 and provides the best estimate based on previous measurements. This represents the *a priori* state estimate:

$$\hat{x}_k^- = E[x(t_k)|y_0, ..., y_{k-1}] \tag{3.19}$$

It should be noted that there is no correlation between the noise evaluated at two different iteration step.
When a new measurement data set is fed to the Kalman filter a new estimate is calculated, named the *a posteriori* state estimate:

$$\hat{x}_k^+ = E[x(t_k)|y_0, ..., y_k] \tag{3.20}$$

Assuming a linear combination between $\hat{x}_k^+$ and $\hat{x}_k^-$, the filter provides the following update relations for state estimate and error covariance. The latter need to be tuned with the measurement error knowledge, based on R_k:

$$\hat{x}_k^+ = \hat{x}_k^- + K_k(y_k - C_k\hat{x}_k^-) = (I - K_kC_k)\hat{x}_k^- + K_ky_k \tag{3.21}$$

$$P_k^+ = (I - K_kC_k)P_k^-(I - K_kC_k)^T + K_kR_kK_k^T \tag{3.22}$$

here the term $(y_k - C\hat{x}_k^-)$ is referred to as *measurement residual*.
The diagonal of the covariance matrix contains the mean squared errors, accordingly the trace[2] is the sum of the mean squared errors:

[2]The trace is the sum of the diagonal element of a matrix

$$P_{kk} = \begin{bmatrix} E[e_{k-1}e_{k-1}^T] & E[e_k e_{k-1}^T] & E[e_{k+1}e_{k-1}^T] \\ E[e_{k-1}e_k^T] & E[e_k e_k^T] & E[e_{k+1}e_k^T] \\ E[e_{k-1}e_{k+1}^T] & E[e_k e_{k+1}^T] & E[e_{k+1}e_{k+1}^T] \end{bmatrix} \tag{3.23}$$

It results that in order to minimize the mean squared error, the trace of P_k has to be minimized, which in turn will minimize the trace of P_{kk}.
The trace of P_k is first differentiated with respect to K_k and set to zero to find the minimum condition. Once solved for K_k the Kalman gain is obtained:

$$K_k = P_k^- C_k^T (C_k P_k^- C_k^T + R_k)^{-1} \tag{3.24}$$

where, as for the state vector, an *a priori* and *a posteriori* covariance estimates are formulated.

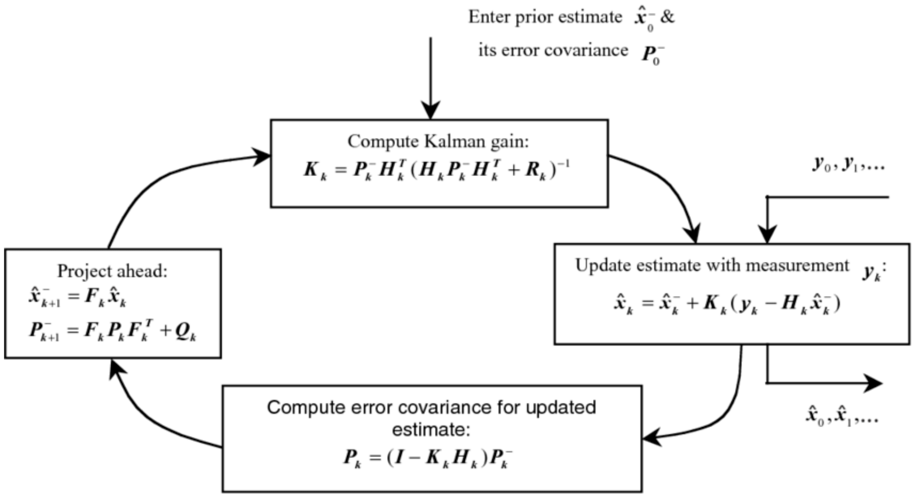

Figure 3.1: Kalman Filter scheme [42]

Some important aspects of Kalman filters should be highlighted. First, since the filter relies on the assumption that disturbances are gaussian distributed, state estimates, true states and state errors will also be described by normal distributions. Because a mean and variance initialization are enough for a normal distribution, the covariance matrix completely describes the error statistics. Second, the gaussian distribution assumption let the Kalman filter operate as an optimal minimum error variance estimator; in case the error follows another statistical distribution, the filter operates as a linear minimum estimator.

3.3.2 Extended Kalman Filter

In order to filter out the noisy measurements, a Kalman Filter has been used and it has proved to a provide good attitude estimation when attitude and attitude rate initial conditions' are small. However, increasing the initial conditions' values, the KF estimate loses accuracy because the S/C system model starts acting nonlinear. Since the system model and measurements functions are quite often nonlinear, different modifications to the KF algorithm have been proposed to handle such nonlinearities. EKF algorithm exploits linear approximations of these functions to compute the state estimates.

In this thesis, the EKF formulation described by Lefferts [9] is adopted. In this case the nonlinear state dynamic is expressed by Eq.3.1:

$$\dot{\hat{x}}(t) = f(\hat{x}(t), u(t), t) + w(t) \tag{3.25}$$

As described for the linear KF, the system will be implemented with a set of initial conditions, adding process' and measurements' gaussian noises.
Again from Eq.3.1, the output vector is given by:

$$y_k = h_k(x(t_k)) + v_k \tag{3.26}$$

Excluding the process noise $w(t)$ from Eq.3.25, the nonlinear system can be integrated to obtain the propagated state vector. Nonlinear state functions are linearized by Taylor series expansions about the state estimate up to the first order terms:

$$F(x(t), t) = f(\hat{x}(t), t) + \frac{\partial f}{\partial x}\Big|_{x=\hat{x}} \Delta x(t) + h.o.t. \tag{3.27}$$

substituting the latter into the covariance propagation equation, also performed trough Taylor series expansion about the local state estimate, a format similar to Eq.3.22 is obtained:

$$\dot{P}(t) = F(\hat{x}(t), t)P(t) + P(t)F^T(\hat{x}, t) + Q(t) \tag{3.28}$$

The main difference is that when using a KF, equations in form of Eq.3.1 are linearized about a predetermined state and the Luenberger gain is calculated, while EKF updates the linearization at each estimation step. So the state matrix A is replaced by the state dynamics Jacobian matrix:

$$F(\hat{x}(t), t) = \frac{\partial f}{\partial x}\Big|_{x=\hat{x}} \tag{3.29}$$

which evaluated the partial derivatives of each of the states.

Since Taylor expansions is the funding element of this algorithm, the truncated terms could cause the filter to diverge if the linearization point is too distant from the true state.

With the same *a priori* and *a posteriori* definitions introduced in the previous section, the update equation of EKF for the state error are given by:

$$\hat{x}_k^+ = \hat{x}_k^- + K_k(y_k - h_k(\hat{x}_k^-)) = (I - K_k h_k(\hat{x}_k^-)) + K_k y_k \tag{3.30}$$

$$P_k^+ = (I - K_k H_k(\hat{x}_k^-))P_k^-(I - K_k H_k(\hat{x}_k^-))^T + K_k R_k K_k^T \tag{3.31}$$

where H_k represent the measurement estimates Jacobian matrix as:

$$H_k(\hat{x}_k^-) = \frac{\partial h_k(x(t_k))}{\partial x(t_k)}\Big|_{x=\hat{x}^-} \tag{3.32}$$

and the Kalman gain is given by:

$$K_k = P_k^- H_k^T(\hat{x}_k^-)(H_k(\hat{x}_k^-)P_k^- H_k^T(\hat{x}_k^-) + R_k)^{-1} \tag{3.33}$$

EKF have some drawbacks, that arise especially when implemented for highly nonlinear system. While for the linear case the optimal Kalman gain is computed from the system matrices as in Eq.3.2, in the nonlinear case the linearization is evaluated within each estimated state vector, rather than around a fixed linearization point. Linearization trough Jacobian matrices is hard and time consuming, besides being computationally expensive when the integration steps are really small. On the other hand, the integration should also be small enough to guarantee filter convergence.
Since the results reliability is strictly related to the Jacobian calculations, a highly accurate system model is mandatory. As a consequence, EKF results to be less robust to parametric or modeling inaccuracies but its estimates are much more reliable. Furthermore state and covariance propagation, independent in the linear Kalman filter formulation, are now coupled. This coupling makes impossible pre-computing the covariances, thus requiring on-board computer to be more loaded.

3.4 Sliding Mode Observers

In the formulation of every simulation model, where discrepancies between the model and the true state will always arise, sliding mode based techniques are one reliable approach to provide robustness, finite-time convergence and reduced-order dynamics in order to reach the desired performances.
Their development was pushed by the dependence of classical observers, such as Kalman filters and Luenberger observers, from the mathematical representation of

the system model. Observers are essentially a mathematical replica of the system accounting for inputs and the differences between estimated and true states. While in the first observers, like Luenberger's, this difference was fed back linearly to the plant, Sliding Mode Observers (SMO) provide the estimation error trough a nonlinear injection term. In presence of unknown signals or uncertainties, this nonlinear feedback could be the key for the observer's convergence in finite time.

Considering the nonlinear dynamic system in Eq.3.1 as introduced in the previous chapters and reported here for simplicity:

$$\begin{aligned} \dot{\mathbf{x}}(t) =& f(\mathbf{x}(t), \mathbf{u}(t), t) + \mathbf{w}(t) \\ \mathbf{y}(t) =& h(\mathbf{x}(t)) + \mathbf{v}(t) \end{aligned} \tag{3.34}$$

The sliding mode observer presented in this thesis work is basically a Luenberger observer made robust and stable against a class of uncertainties and neglected nonlinearities using a signum or relay function [25] [28]. In this formulation, $f(\mathbf{x}(t), \mathbf{u}(t), t)$ and disturbances are unknown but assumed to be upper bounded by a continuous function of x and t.

3.4.1 Introduction to Sliding Mode Techniques

A practical example is introduced to better describe the sliding mode principles. Considering a simple system state-variable description, position and velocity can be formulated as:

$$\begin{cases} \dot{x}_1 = x_2 \\ \dot{x}_2 = u + f(x_1, x_2, t) \end{cases} \tag{3.35}$$

with known initial conditions $x_1(0) = x_{1_0}$ and $x_2(0) = x_{2_0}$.
The original system can be associated to the following compensated dynamic, in which no disturbance is injected:

$$\dot{x}_1 + \lambda x_1 \qquad \text{with} \qquad \lambda > 0 \tag{3.36}$$

The general solution of the latter equation is, in its standard form:

$$x = x_0 e^{-\lambda t} \tag{3.37}$$

that converges for positive value of λ.

The funding idea behind sliding-mode based techniques is to use a discontinuous switching control law, instead of using a continuous formulation, to tailor a particular desired state while rejecting uncertainties of the systems. This control acts to guide the system state propagation along a *sliding surface*, generally defined as:

Figure 3.2: The sliding condition [24]

$$S = \{x : \sigma(x) = 0\} \tag{3.38}$$

since $x_2(t) = \dot{x}_1(t)$, it's possible to define the sliding variable as:

$$\sigma = \sigma(x_1, x_2) = x_2 + \lambda x_1 \qquad \text{with} \qquad \lambda > 0 \tag{3.39}$$

where $\sigma(x)$ is the sliding variable and S represents a reduced order motion of the system dynamic.
In order to achieve asymptotic convergence to the true states in presence of bounded disturbances, i.e. driving the variable σ to zero, Lyapunov function techniques are applied to the σ-dynamics:

$$\dot{\sigma} = \lambda x_2 + f(x_1, x_2, t) + u \qquad \text{with} \qquad \sigma(0) = \sigma_0 \tag{3.40}$$

With this formulation, a candidate Lyapunov functions can be written in the following form [43]:

$$V = \frac{1}{2}\sigma^2 \tag{3.41}$$

Providing asymptotic stability requires to comply with the two following conditions:

$$\begin{array}{llll} \mathbf{1}. & \Rightarrow & \dot{V} < 0 & for\ \sigma \neq 0 \\ \mathbf{2}. & \Rightarrow & \lim\limits_{|\sigma| \to \infty} V = \infty & \end{array} \tag{3.42}$$

While the first condition is intrinsically verified by Eq.3.41, the second one can be reformulated as:

$$\dot{V} = -\alpha V^{1/2} \qquad \text{with} \qquad \alpha > 0 \tag{3.43}$$

The latter equation represent the *reachability condition* and guarantees that once reached the sliding surface, the variable evolves along it. This condition is equivalent to:

$$\sigma\dot{\sigma} \leq \frac{\alpha}{\sqrt{2}}|\sigma| \tag{3.44}$$

Time-integrating Eq.3.43 equation and setting $V(t)$ to reach zero, finite time of converge is obtained:

$$t_r \leq \frac{2V^{1/2}(0)}{\alpha} \tag{3.45}$$

where the larger is α, the faster the variables will reach the sliding surface.
The control input function will drive the sliding surface to the desired condition only when it complies with Eq.3.43, such that outside of $s(t)$:

$$\frac{1}{2}\frac{d}{dt}\sigma^2 \leq -\rho|\sigma| \quad \rho > 0 \tag{3.46}$$

where, the value of ρ is obtained trough Lyapunov stability condition ($V = \sigma^2$):

$$\sigma\dot{\sigma} = -\rho|\sigma| \quad \Rightarrow \quad \dot{\sigma} = -\rho sgn(\sigma) \tag{3.47}$$

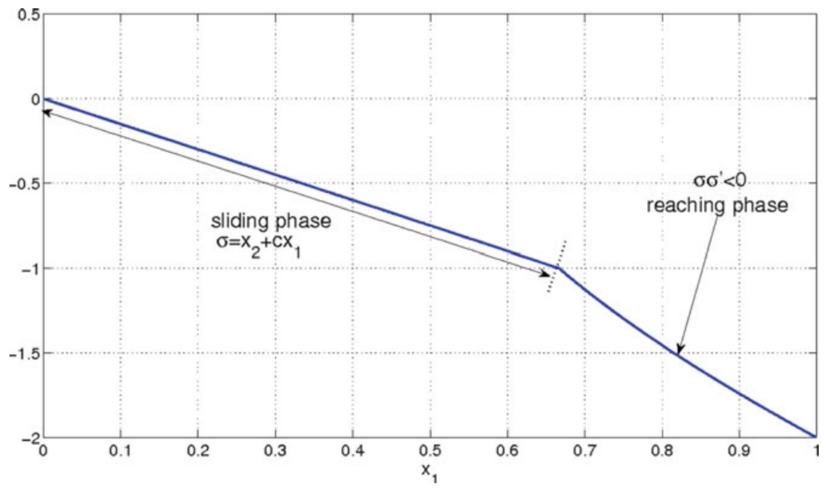

Figure 3.3: SMO phase portrait [43]

Then, considering the following input:

$$u = -\lambda x_2 - \rho sgn(\sigma) \tag{3.48}$$

where $sgn(\sigma)$ refers to the sliding surface's signum, the cause of sliding mode being discontinuous, and can be defined as:

$$sgn(x) = \begin{cases} 1 & \text{if } x > 0 \\ -1 & \text{if } x < 0 \end{cases} \tag{3.49}$$

In order to completely understand the SMO fundamentals, a typical phase portrait analysis is reported in figure 3.3.
It's possible to distinguish two different behaviors of the system dynamic. Firstly, the state condition is driven towards the sliding surface in the *reachability phase*. Then the system state is driven towards the origin, constrained along the sliding surface in the *sliding phase*. For the considered system the desired condition is the null vector.
Since in an ideal sliding mode the switching frequency is supposed to be infinity, the discrete time nature, i.e. finite frequency available, by the simulation conditions could cause some *chattering* during the sliding mode, merely a zigzag motion in small amplitude and high frequency of the variables. Higher the sliding mode frequency, lower the zigzag effect would be.

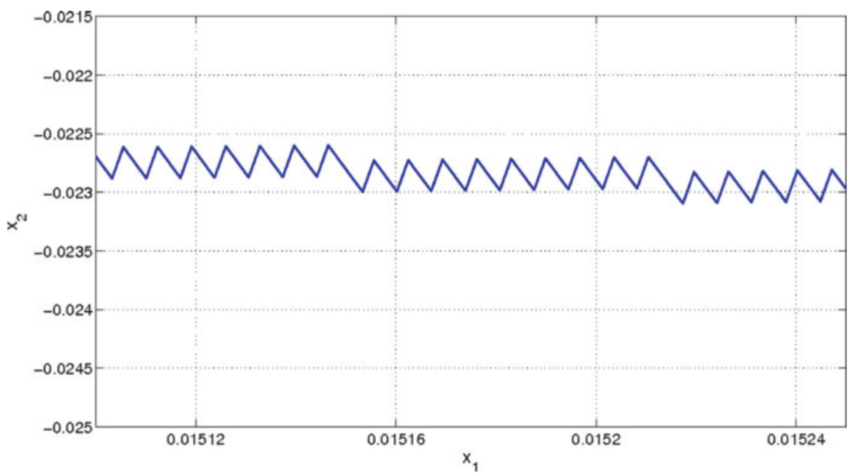

Figure 3.4: SMO phase chattering [43]

However, a sliding surface defined as in Eq.3.39 is not exploitable when some states are unavailable for measurement. In reference [24] proposed a second order observer with multi input and multi output states to handle this problem.

3.4.2 First order Sliding Mode Observer

The observer model adopted assumes a nonlinear, observable system with a linear measurement formulation

$$\begin{aligned} \dot{\mathbf{x}}(t) &= f(\mathbf{x}(t), \mathbf{u}(t), t) \\ \mathbf{y}(t) &= C(t)\mathbf{x}(t) + \mathbf{v}(t) \end{aligned} \tag{3.50}$$

Having introduced the characterizing element of techniques based in the sliding mode, a few assumptions should be pointed out to utilize them as observers.
Let $\mathbf{z}$ be an auxiliary sliding variable defined as an estimation error between the estimated and true system state:

$$\tilde{\mathbf{z}} = \mathbf{z} - \hat{\mathbf{z}} \tag{3.51}$$

Assuming the variable to be estimated as bounded by some known and small values, the observer injection therm can be defined as:

$$\dot{\hat{z}} = \nu = -\rho sgn(z) \tag{3.52}$$

The considered approach involves the study of the spacecraft attitude system with decoupled axes, where three sliding observers are run in parallel using a linearized model of the system for the observer dynamics [28].

Similarly as what introduced for the Kalman filters, consider the nonlinear system dynamic as defined in Eq.3.1, assembled with spacecraft's kinematic and dynamics equations and combined with parametric uncertainties.
The observer model is formulated as:

$$\begin{aligned} \dot{\mathbf{x}} = [\mathbf{f}(x,t) + \Delta\mathbf{f}(x,t)] + [B + \Delta B][\mathbf{u}(t) + \Delta\mathbf{u}] + \mathbf{T}(t) \\ \mathbf{y} = C\mathbf{x} + \nu \end{aligned} \tag{3.53}$$

where the state propagation is defined from:

$$\mathbf{f}(x,t) = \begin{bmatrix} ((I_y - I_z)/I_x)\omega_y\omega_z \\ ((I_z - I_x)/I_y)\omega_x\omega_z \\ ((I_x - I_y)/I_z)\omega_x\omega_y \\ -0.5(\omega_x q_1 + \omega_y q_2 + \omega_z q_3) \\ 0.5(\omega_x q_0 + \omega_z q_2 - \omega_y q_3) \\ 0.5(\omega_y q_0 - \omega_z q_1 + \omega_x q_3) \\ 0.5(\omega_z q_0 + \omega_y q_1 - \omega_x q_2) \end{bmatrix} \tag{3.54}$$

Here the state vector is a seven-dimension column vector, composed by the attitude body rate as the first three elements and quaternions as the last four. $\mathbf{B}$ is defined as $\mathbf{B} = [\mathbf{J}^{-1}\ \mathbf{0}^{4x3}]'$, $\mathbf{u}(t)$ represents the control torques acting on the vehicle and $\mathbf{T}(t)$ include every torque acting on the vehicle. In addition the Δ terms takes

into account modeling errors, parameters uncertainties and control inaccuracies.
The sliding observer is implemented on the nonlinear dynamic and kinematic equations of motion to obtain the angular rate and attitude estimates. SMO uses continuous state propagation with discrete measurement corrections to estimate quaternions and angular rates. Uncertainties terms reconstruction is one of the benefits of SMOs over Luenberger-like observer.
With these assumptions, the SMO presented in this thesis has the following form:

$$\begin{aligned} \dot{\hat{\mathbf{x}}} &= \mathbf{f}(\hat{\mathbf{x}}, t) + B\mathbf{u}(t) + H[\mathbf{y} - \hat{\mathbf{y}}] + \mathbf{K}sat\left(\frac{\mathbf{z}}{\boldsymbol{\phi}}\right) \\ \hat{\mathbf{y}} &= C\hat{\mathbf{x}} \\ \tilde{\mathbf{y}} &= \mathbf{y} - C\hat{\mathbf{x}} \end{aligned} \tag{3.55}$$

where $\mathbf{H}$ and $\mathbf{K}$ are the corresponding Luenberger's and switching gain, respectively, and $\boldsymbol{\phi}$ is the boundary layer vector.
The most time requiring process in the Sliding Mode Observer design is the gains' tuning. Several simulations have showed that while the Luenberger correction term affects the estimates' time of convergence, the switching gains should be minimized to guarantee convergence under given uncertainties. The boundary layer thickness value, whose purpose is to relax the zero condition on the sliding surface, is limited by the magnitude of measurement noise.

The introduction of a high frequency nonlinear switching function drives the error between the actual and estimated state to zero, enhancing the robustness of the observer but also increasing the nonlinearity of the system. To reduce this problem it's possible to act in two ways: firstly fixed gain SMO are used, secondly to minimize chattering noise caused by the $sgn(x)$ function, a saturation function is implemented as:

$$sat(x) = \begin{cases} 1, & x > \phi \\ x/\phi, & |x| < \phi \\ -1, & x < -\phi \end{cases} \tag{3.56}$$

As previously mentioned, in order to set a sliding surface, an observer error should be defined. The angular rate error is simply computed with the algebraic difference between the measured and observer values. Instead quaternion correction can be performed in two different ways:

- **Additive Correction**: This approach formulate quaternion correction simply trough algebraic difference between measured and estimated quaternion:

$$\tilde{\mathbf{y}} = \mathbf{S} = \mathbf{q}_m - \tilde{q} \tag{3.57}$$

After correction quaternion normalization is performed according to:

$$\tilde{\mathbf{q}}_{norm}(t) = \frac{\hat{\mathbf{q}}(t)}{|\hat{\mathbf{q}}(t)|} \tag{3.58}$$

- **Multiplicative Correction**: This approach may be more suited because it complies with quaternion properties. In this case the quaternion error is formulated considering quaternion multiplication between the measured state and the inverse observed quaternion:

$$\tilde{\mathbf{q}} = \mathbf{q}_m \otimes \hat{\mathbf{q}}^{-1} \tag{3.59}$$

  In the implemented SMO, both correction have been tested without any relevant difference but a faster algorithm execution in case of multiplicative correction. For this reason the second approach have been implemented for simulations.

Unlike the EKF, the SMO requires no linearization during the estimation process, making it more robust to uncertainties.
Observers aim to reduce the computational load of traditional filters, such as the EKF, without degrading the reliability of the output data in presence of uncertainties, measurement noises and disturbances.

3.5 Sensors mathematical framework

In this section the general mathematical models for star trackers and gyroscopes are presented. The two set of measurements are implemented in the output matrix $\mathbf{H} \in \mathbf{R}^7$, defined from Eq.3.2:

$$\mathbf{y}_k = \begin{bmatrix} \mathbf{y}_{gyro_k} \\ \mathbf{q}_{str_k} \end{bmatrix} = \begin{bmatrix} \boldsymbol{\omega}_{B_{meas}} \\ \mathbf{q}_{meas} \end{bmatrix} = \begin{bmatrix} H_{gyro} \\ H_{str} \end{bmatrix} \mathbf{x}_k + \begin{bmatrix} \boldsymbol{\nu}_{gyro} \\ \boldsymbol{\nu}_{str} \end{bmatrix} \tag{3.60}$$

In space there are several sources of noise that change drastically and with different frequencies and can thus be unpredictable. For this reason, noise modeling is a difficult task and should be carried out stochastically with an accurate knowledge of the sensors and of the environment in which the spacecraft operates.

3.5.1 Star tracker measurement model

Space Rider is equipped with a set of three new star tracker architecture: SPACESTAR *(Satellite Platform Avionics Computer Embedding Star Tracker Algorithms And Resources)*, two located in the AVUM module and the other one in the cargo bay. SPACESTAR is a medium FoV star tracker, composed by up to three optical heads, each of them containing a baffle, an optical system, a focal plane, proximity electronic and a software running in the Attitude Control System on-board computer. This platform handles the complete process from compressed sky images to quaternion solution enabling to get rid of unnecessary redundant hardware, such as star catalogs or DC/DC converters.

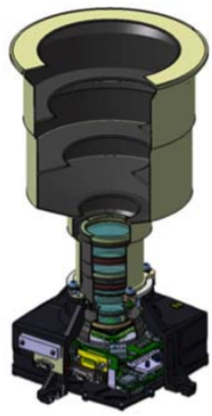

Figure 3.5: SPACESTAR Optical Head Cutaway View [44]

SPACESTAR design is based on the already qualified AA-STR which features robust and accurate three axis attitude determination with very limited mass budget and power consumption with an improved radiation hardening case. The embedded software is executed periodically by the AOCS, providing an update rate up to 10 Hz and monitors each of the optical heads, bypassing its data if one of them becomes unreliable.
The STR has two main operative modes, depending on the S/C angular rate:

- Normal Mode (for low-medium angular rate up to 1.5 deg/sec)
- High Angular Rate Mode (for high angular rate)

For simulation purposes, star trackers are assumed to be in Normal Mode. In this operative condition each optical head tracks $8-9$ stars (depending on the CPU budget), computes the quaternion solution and performs data fusion with the other attitude measurements, also providing autonomous calibration for misalignments. Initial errors such as optical offset and thermo-elastic structural deformation can be present for multiple reasons, such as: procedures errors during vehicle assembly, integration and verification, a harsh environment once in orbit and strong vibrations during launch. Indeed during a typical space mission, at a certain point of spacecraft's assembly and integration phases, some instruments could become unaccessible. Thus the last sensors' orientation assessment represents the pre-flight knowledge of the star trackers' orientation and the baseline to evaluate any kind of misalignments.

In the standard configuration, two star trackers will be mounted on the AVUM orbital module pointing as in Fig. 3.6.
Eventually a third star sensor will be mounted over the reentry module IMU to increase the overall sky coverage.

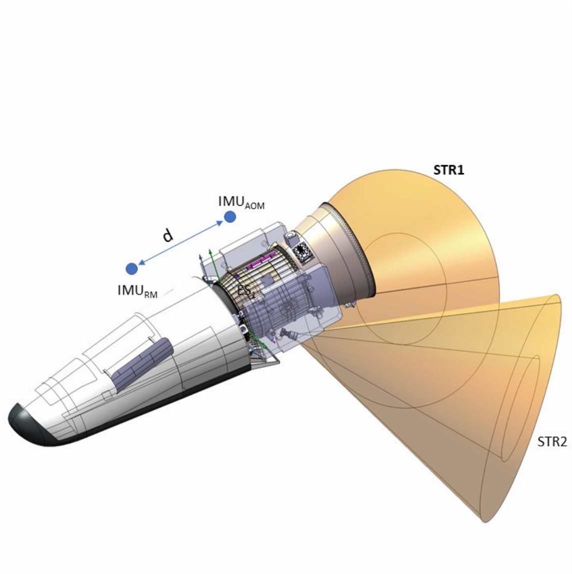

Figure 3.6: AVUM orbital module star trackers [45]

Attitude measurements are sampled w.r.t the reference frame of a single SPACESTAR optical head, defined as a master reference. The other star trackers measurements are projected into this master reference trough alignment matrices (ground measured or on-board estimated), fused at quaternion level and then rotated into the LVLH frame. Since the combination of offsets becomes unobservable if misalignments are modeled in all the attitude sensors onboard a spacecraft, it's common practice to eliminate one rotational misalignment assuming one sensor as a master reference [46].

Let s, s_0, B, eci denote the star tracker real and nominal frame, body frame and the inertial ECI frame. The angular displacement between the real and nominal frame is referred to as misalignment.
Considering the nominal mounting directions described by Eq.2.4 and Eq.2.5, that define the orientation of a nominal sensor frame s_b^0 with respect to the body frame, the transformation from body reference to true sensors orientation can be written trough quaternion rotations as:

$$\mathbf{q}_{eci}^{s} = \mathbf{q}_{s_0}^{s} \otimes \mathbf{q}_{b}^{s_0} \otimes \mathbf{q}_{eci}^{b} \tag{3.61}$$

here $\mathbf{q}_j^i$ indicates the quaternion rotation from the *i-frame* to *j-frame*.
For in-flight misalignments, caused by thermal variations outside the operative limits, radiation aging and other factors, the deviation error from the nominal mounting position of the star tracker is limited and can be approximated as:

$$\delta\mathbf{q} = \begin{bmatrix} 1 \\ \boldsymbol{\delta}_{STR} \end{bmatrix} \simeq \frac{1}{2} \begin{bmatrix} \psi_{err} \\ \theta_{err} \\ \phi_{err} \end{bmatrix} \tag{3.62}$$

where $\boldsymbol{\delta}_{STR}$ is a three dimensional vector with random nature to be estimated.

3.5.2 Sources of Errors

Over the past few decades, the measurement error of the star sensor has been often simplified as white noise. However, in cases where high accuracy attitude determination performance is required, this simplification is not valid anymore [47]. As a matter of fact, star sensors are subjected to different sources of error: *bias, low frequency error* and *noise* itself.

In normal mode, the following bias values can be considered

- Pitch/Yaw: 8 arcsec (3σ)
- Roll: 11 arcsec $3(\sigma)$

Bias errors can be further divides in a low and in a high frequency error.
Low frequency errors are function of the optical heads mutual orientation and local misalignments stability, i.e. boresight and mounting baseplate stability. Their value also depend on the operating temperature range as in Table 3.1.

Low Frequency Error		
Baseplate Temperature Range	**Error**(3σ) **Pitch/Yaw**	**Error**(3σ) **Roll**
$\pm 5°C$ around T_{nom}	2.5 *arcsec*	4.5 *arcsec*
From $-25°C$ *to* $\pm$ $50°C$	10.2 *arcsec*	4.9 *arcsec*

Table 3.1: STR Low Frequency Error

High frequency errors result from the optical heads' data fusion. In normal mode, the bias values reported in Table 3.2 can be considered.

To guarantee high accuracy performance during the entire mission, it's necessary to account for misalignments, such as lens distortion or sensor alterations, due by the environmental changes throughout the entire mission envelope. In particular the launch and ascent phases are the most extreme for on-board sensors: vibrations, thermal fluxes over the vehicle and the shock caused by the stages separation are

High Frequency Error			
Spacecraft Rate	**X** $(arcsec, 3\sigma)$	**Y** $(arcsec, 3\sigma)$	**Z** $(arcsec, 3\sigma)$
0.1 deg/sec	7.5	8.4	7.2
0.5 deg/sec	10.8	11.6	9.9
1 deg/sec	17.3	18.6	15.9
4 deg/sec	45	45	45

Table 3.2: STR High Frequency Error

likely to cause damages. Furthermore as the spacecraft orbits around the planet, or travel trough space, it may encounter different illuminating condition and experience huge temperature variations. Moreover other systematics errors come from the instruments' components aging.

In order to achieve high precision attitude determination, star trackers should be able to perform autonomous self-calibration in orbit, providing a reliable solution of the lost-in-space problem as well as a recursive attitude estimation process. The attitude estimation process must be executed multiple times during the operational life of the spacecraft, minimizing the time and power required.

3.5.3 Gyroscope measurement model

As inertial instruments and since they are composed by mechanical parts, strapdown gyros are affected by several types of noises, such as electronic noise, flat torque noise and float acceleration. The noises generate mainly three types of errors: a low frequency time-varying component, referred to as *gyro bias* β_g, *a time invariant white noise* η_1, modeled as a zero mean Gaussian variable and the *drift-rate* $\dot{\beta}$, modeled as a random walk process η_2.
Generally Rate Random Walk (RRW) and Angular Random Walk (ARW) errors variances are computed trough the Allan Variance Diagram. These parameters define the quality of the sensors, in particular in terms of bias rate of change and white errors magnitude. Obviously a high quality gyro provides reliable measurements for a longer period than low quality gyro.
The assumptions of uncorrelated white noise processes allows to treat each axis separately and enables to adopt a widely used three-axis continuous time mathematical model for a rate integrating gyro is given by [4]:

$$\boldsymbol{\omega}^{meas} = (1+k)\boldsymbol{\omega}^{true} + \boldsymbol{\beta}_g + \boldsymbol{\eta}_1 \tag{3.63}$$

$$\boldsymbol{\beta}_g = \eta_2 \tag{3.64}$$

where k is a small correction to the nominal scale factor, due to rate and rate-integrating gyro factors, $\boldsymbol{\beta_g}$ is the drift rate, $\boldsymbol{\eta}_1$ and $\boldsymbol{\eta}_2$ are independent zero-mean Gaussian white-noise processes.
In the Kalman filter's propagation equations, Eq.3.63 is assumed to be integrated discretely, since in practice rate-integrating gyros are used, which compute the S/C angular rates continuously but samples at discrete intervals. The S/C attitude is also propagated at the same time step, or multiple, as the gyros'. If the attitude update interval is much shorter than the Kalman filter update interval, the approximation of continuous gyro holds.
In order to reduce the computational load of the measurements' process, the continuos-time gyro formulation is converted into a discrete-time one:

$$\boldsymbol{\omega}_{k+1}^{meas} = \boldsymbol{\omega}_{k+1}^{true} + \frac{1}{2}(\boldsymbol{\beta}_{k+1}^{true} + \boldsymbol{\beta}_k^{true}) + \sqrt{(\frac{\sigma_1^2}{\Delta t} + \frac{1}{12}\sigma_2^2\Delta t)}N_1 \tag{3.65}$$

$$\boldsymbol{\beta}_{k+1}^{true} = \boldsymbol{\beta}_k^{true} + \sqrt{\sigma_2\Delta t}N_2 \tag{3.66}$$

where k is the time step, Δt is the gyro sampling interval, $\boldsymbol{\sigma}_1$ and $\boldsymbol{\sigma}_2$ are the spectral densities of the Gaussian white noise processes $\boldsymbol{\eta}_1$ and $\boldsymbol{\eta}_2$ respectively. N_1 and N_2 are the zero mean random variables with unity variance.

Chapter 4

Simulation results

A comparison via numerical simulations is made of Sliding Mode Observer versus Kalman Filter in the attitude estimation framework of Space Rider. The simulations run in this thesis work set the attitude of Space Rider as an Earth pointing spacecraft. In this case the body local frame overlaps the LVLH frame and the unit quaternion is assumed as the desired attitude.

4.1 Numerical Simulation

Since the simulations include random noises in the system dynamic and in the measurement process, the filters performance need to be analyzed with statistically random input noises.
Because the objective of this thesis was not to assess the control system robustness, the simulations have been run feeding the guidance systems with the true states rather than with the noisy ones, even if observer based controller performance were somehow evaluated.

The inertial properties of space rider are embedded in the inertia matrix as defined in Eq.2.37, that, for simulation related purposes, is considered diagonal with the following components:

$$\mathbf{J} = \begin{bmatrix} 3000 & 0 & 0 \\ 0 & 21000 & 0 \\ 0 & 0 & 20000 \end{bmatrix} kg \cdot m^2 \tag{4.1}$$

The Kalman gain for the filters is found trough minimization of a cost function and selection of non-zero weighting matrices $\mathbf{Q}$ and $\mathbf{R}$. Since the state vector is composed by quaternions and angular rates, these matrices should be positively defined and designed partitioning the elements which are directly available for measurements.

If the knowledge on the initial conditions values is accurate, the initial state estimation error covariance is set to a small value. Otherwise if the initial state values confidence is low, the error covariance should be set to a higher value.
For the following simulations:

$$P_0 = \begin{bmatrix} 10^{-6} & 0 & 0 & 0 & 0 & 0 & 0 \\ 0 & 10^{-6} & 0 & 0 & 0 & 0 & 0 \\ 0 & 0 & 10^{-6} & 0 & 0 & 0 & 0 \\ 0 & 0 & 0 & 10^{-6} & 0 & 0 & 0 \\ 0 & 0 & 0 & 0 & 10^{-6} & 0 & 0 \\ 0 & 0 & 0 & 0 & 0 & 10^{-6} & 0 \\ 0 & 0 & 0 & 0 & 0 & 0 & 10^{-6} \end{bmatrix} \tag{4.2}$$

Multiple scenarios have been tested. For the ideal case, i.e. where the initial conditions are set to small values, the Kalman filter behaves essentially like its extended form and the two curves collapse converging immediately. For simplicity these simulations results are not reported.

The SMO gains have been tuned after several simulations in order to obtain the best steady state performances. The chosen values are:

$$\begin{aligned} \mathbf{H}_\omega &= \begin{bmatrix} 0.005 & 0.005 & 0.005 & 0.001 & 0.001 & 0.001 & 0.001 \end{bmatrix}' \\ \mathbf{H}_\mathbf{q} &= \begin{bmatrix} 10 & 10 & 10 & 10 & 10 & 10 & 10 \end{bmatrix}' \end{aligned} \tag{4.3}$$

with a boundary layer value set to $\phi = 0.003$.
Globally it results that the Luenberger correction term helps to increase the convergence rate. However it's also possible to obtain sufficient accuracy, but in a longer period, only with the saturation correction.

4.1.1 Case 1 - Small attitude rate initial error with small offset

The first case of study is a simulation where the initial conditions of the dynamics are set to a casual orientation for attitude and a low attitude rate:

$$\begin{aligned} \mathbf{q}(0) &= \begin{bmatrix} 0.2 & 0.3 & 0.6 & 0.8 \end{bmatrix}' \\ \boldsymbol{\omega}_{\boldsymbol{B}}(0) &= \begin{bmatrix} 0.02 & 0.02 & 0.02 \end{bmatrix}' \end{aligned} \tag{4.4}$$

while the filters' and SMO's are:

$$\begin{aligned} \mathbf{q}_{smo}(0) =& \mathbf{q}_{KF}(0) = \mathbf{q}_{EKF}(0) = \begin{bmatrix} 0 & 0 & 0 & 0 \end{bmatrix}' \\ \boldsymbol{\omega}_{\boldsymbol{B}smo}(0) =& \boldsymbol{\omega}_{\boldsymbol{B}KF}(0) = \boldsymbol{\omega}_{\boldsymbol{B}EKF}(0) = \begin{bmatrix} 0 & 0 & 0 \end{bmatrix}' \end{aligned} \tag{4.5}$$

The first three plots describe the attitude rate and orientation, in terms of quaternions and Euler angles.

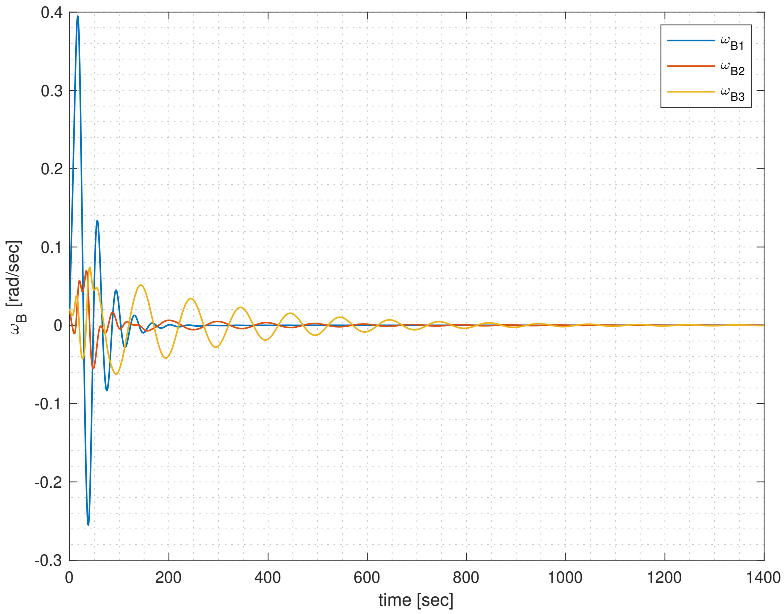

Figure 4.1: Case 1: True attitude rate

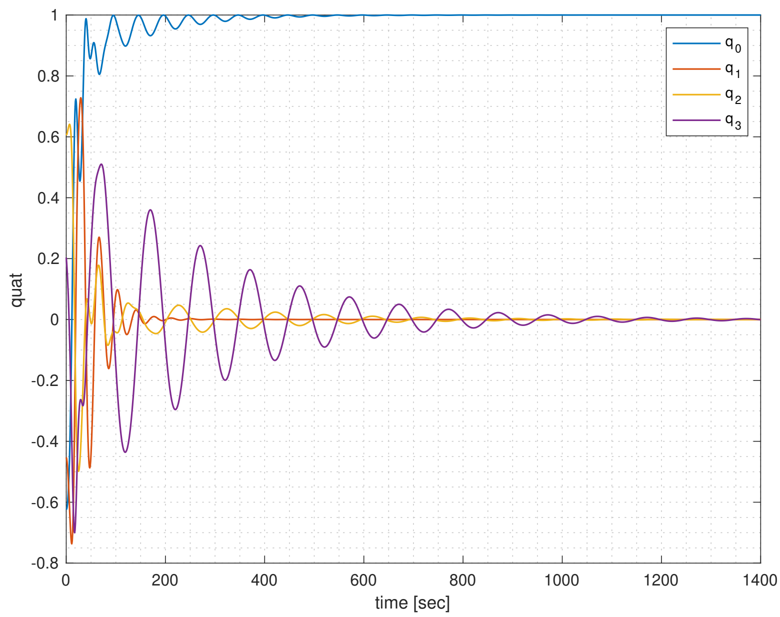

Figure 4.2: Case 1: True attitude quaternions

From the dynamics of the spacecraft, the controller acts correctly driving the attitude to the unit quaternion, i.e. aligning its body axes to the LVLH system and

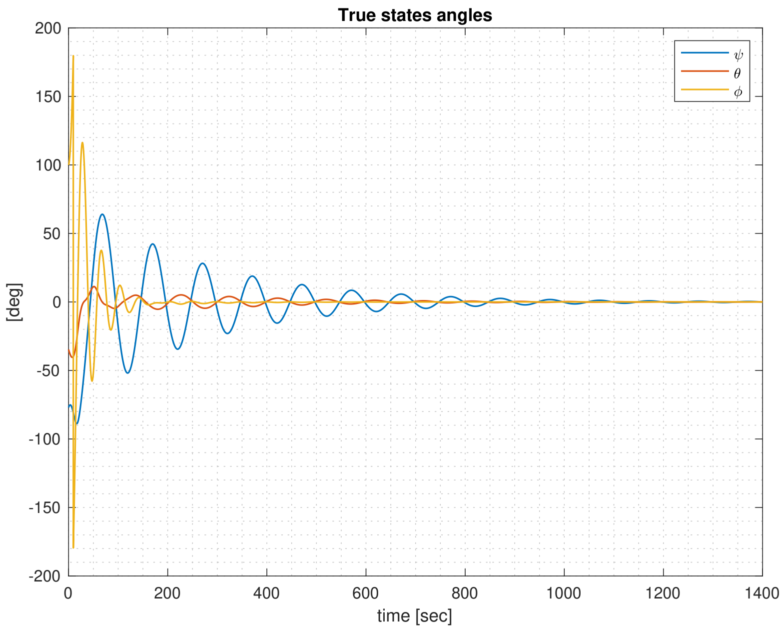

Figure 4.3: Case 1: True attitude angles

stabilizing its motion in finite time.

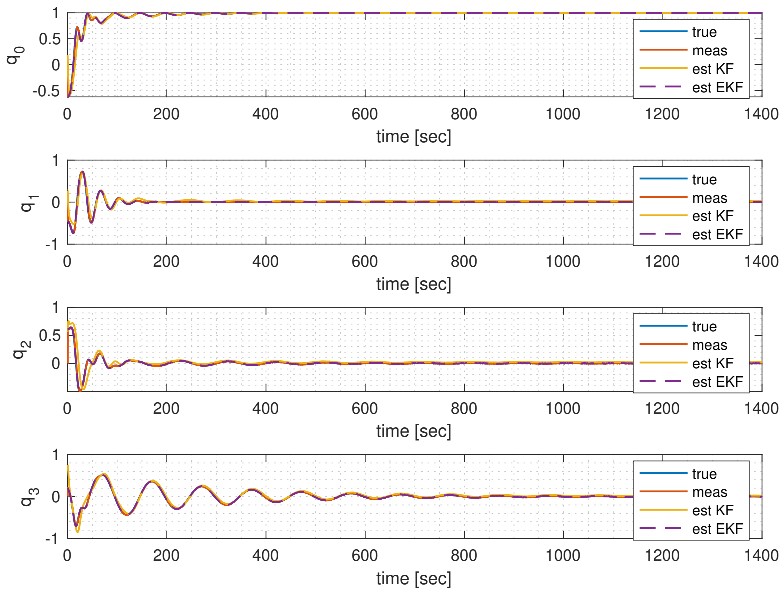

Figure 4.4: Case 1: Quaternions estimation trough KF + EKF

The states estimation is performed trough KF and EKF and the results are reported in figures Fig 4.4 and Fig 4.5.

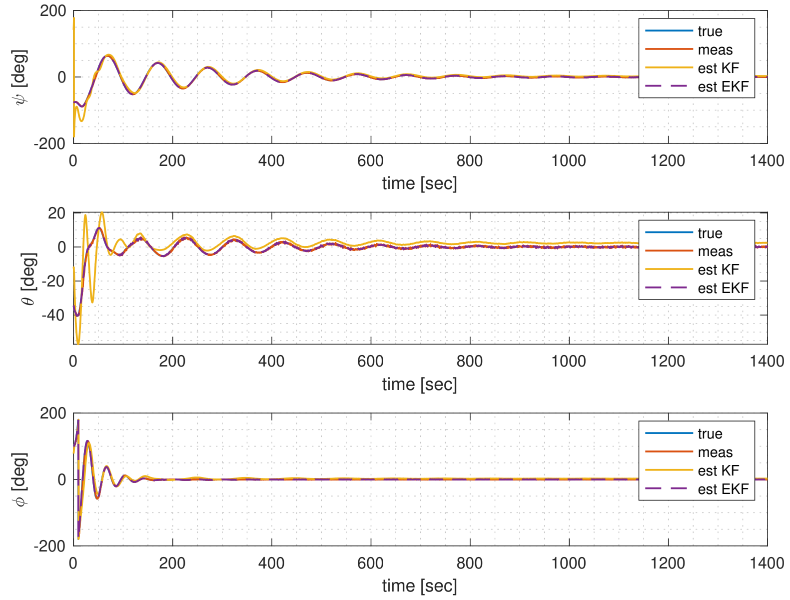

Figure 4.5: Case 1: Angles estimation trough KF + EKF

From the attitude estimation results, expressed in Euler angles, it results that the Kalman filter is unable to converge to the real states and a big steady state error is still present.

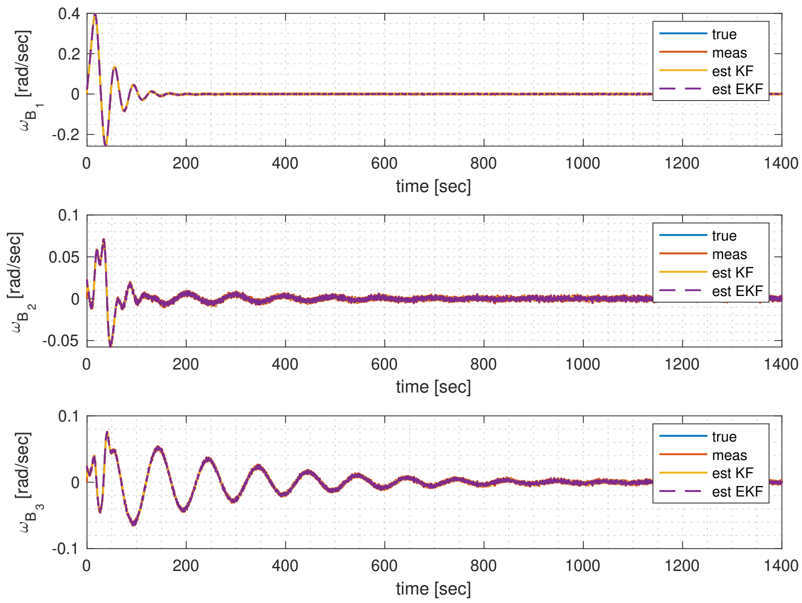

Figure 4.6: Case 1: Attitude rates estimation trough KF + EKF

Attitude rate estimation is reported in Fig 4.6.

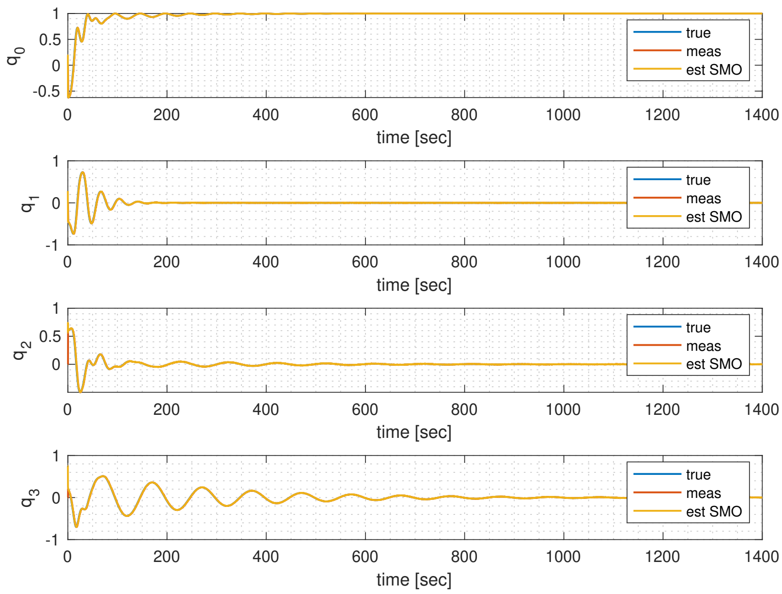

Figure 4.7: Case 1: Quaternion estimation trough SMO

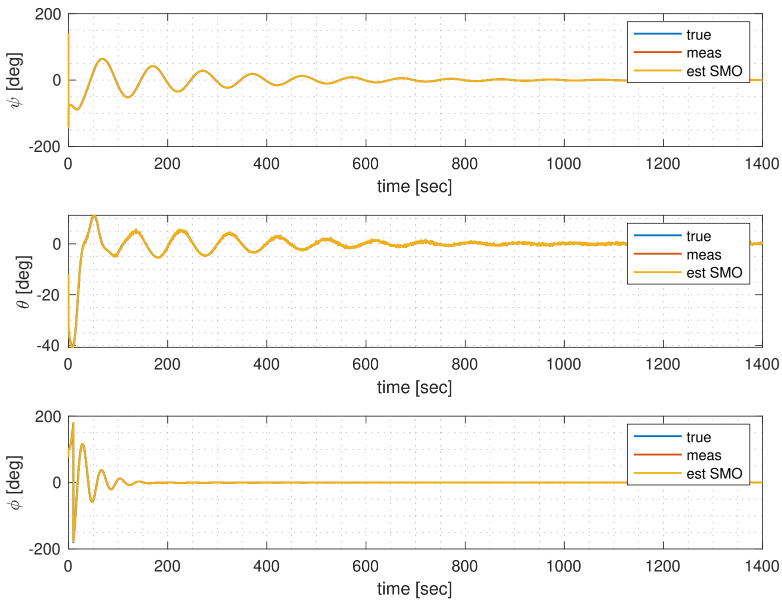

Figure 4.8: Case 1: Euler angles estimation trough SMO

The SMO based attitude, reported using the quaternion representation in Fig 4.7 and the Euler angles one in Fig 4.8 and attitude rate estimation Fig 4.9. However, in order to better understand the performances of the algorithms, the attitude error, index of the overall accuracy, has been also reported in Fig 4.10.

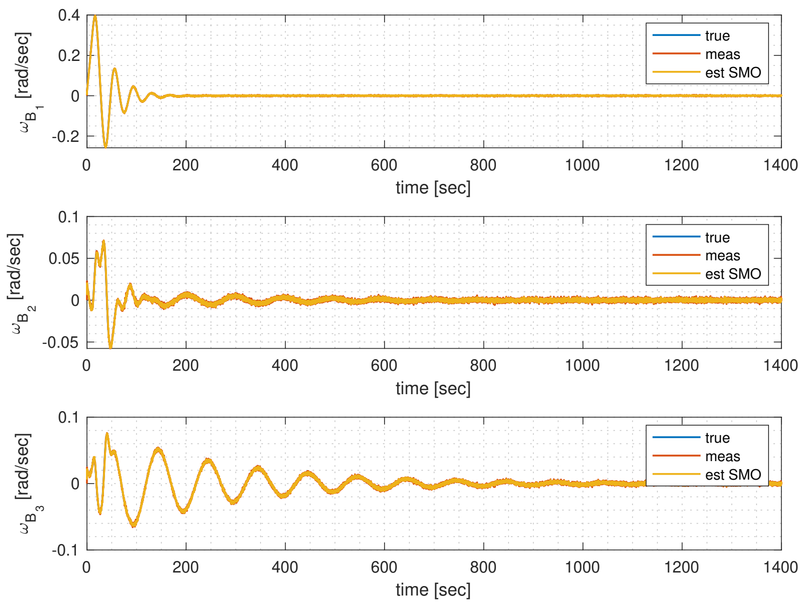

Figure 4.9: Case 1: Attitude rates estimation trough SMO

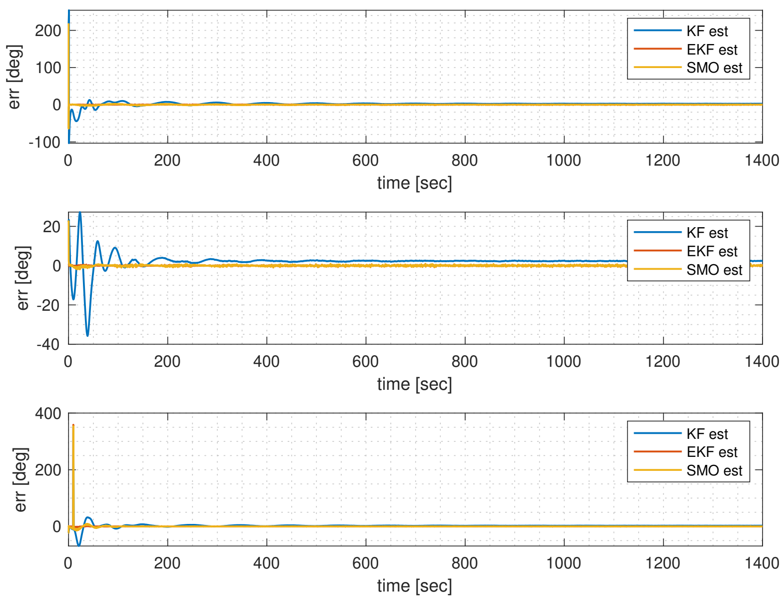

Figure 4.10: Case 1: Attitude errors KF + EKF + SMO

The observer converges to the real states without any big steady state error. In order to guarantee convergence, state vector components are assumed to be bounded to 1 rad. Since Space Rider is a three axis stabilized spacecraft, nominal angular velocities should lie in a range below 1 rad/s.

While the linear Kalman filter is unable to achieve convergence, as previously mentioned, the EKF and SMO appear to drive the error to zero. Zooming into the last part of the graph, it's possible to see that, even if the EKF remains less stable at steady state, it has better accuracy. In particular the error for SMO reduces to 0.02° and for EKF it reaches 0.0026°.

Finally, from the estimates errors, it's possible to estimate the sensors offsets. Star trackers misalignments reconstruction is carried out trough the filters attitude estimates, projecting back the measurements in the inertial frame and comparing them with the measurements expected from the orientation knowledge of the sensor, in the same fashion as defined in Eq.3.62.

Thus quaternion misalignments can be expressed as:

$$\mathbf{q}_{mis} = \mathbf{q}_{nom}^{-1} \otimes \mathbf{q}_{est} \tag{4.6}$$

where $\mathbf{q}_{nom}^{-1}$ is the measurement quaternion inverse as expected from the STR in the nominal position and $\mathbf{q}_{est}$ is the attitude quaternion estimated from the filter in analysis.

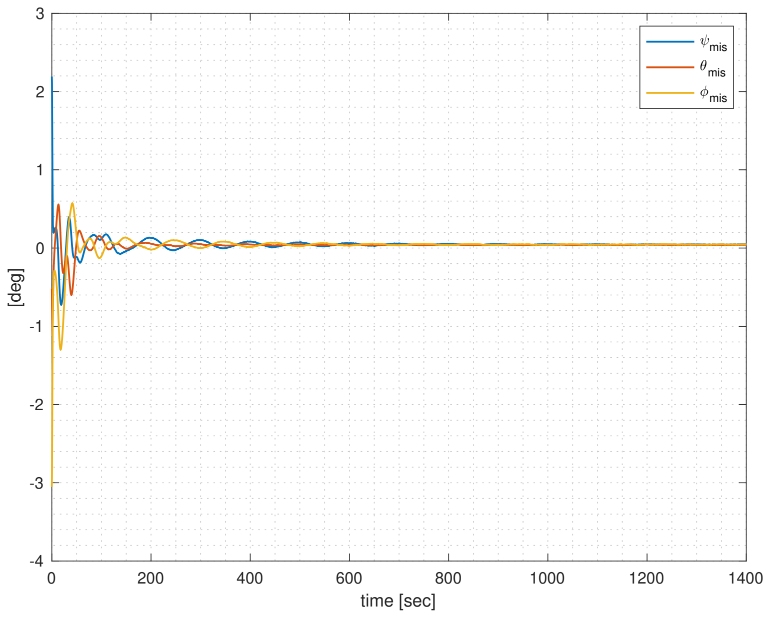

Figure 4.11: Case 1: Star tracker misalignments estimation KF

The misalignments estimations of KF, EKF and SMO are reported in Fig 4.11, Fig 4.12 and Fig 4.13, respectively.
The steady state estimation trough SMO are the only one to converge to some values that in this case are:

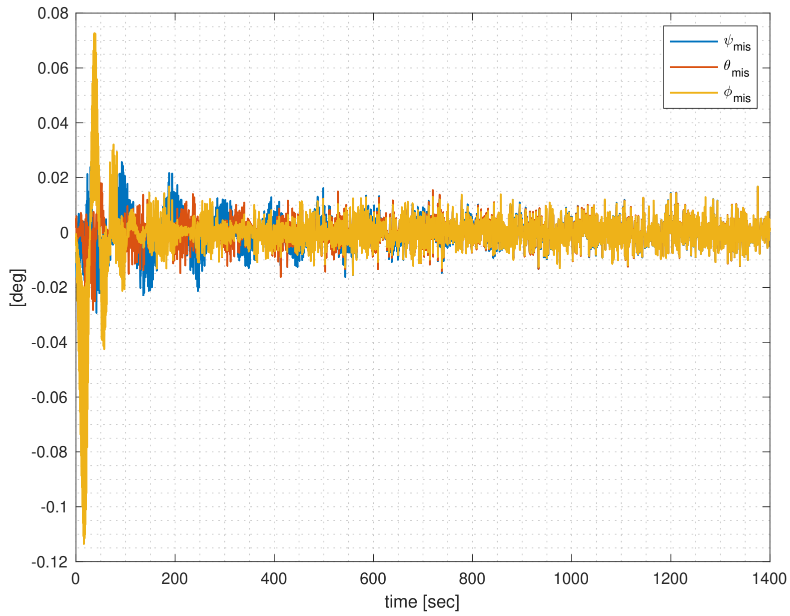

Figure 4.12: Case 1: Star tracker misalignments estimation EKF

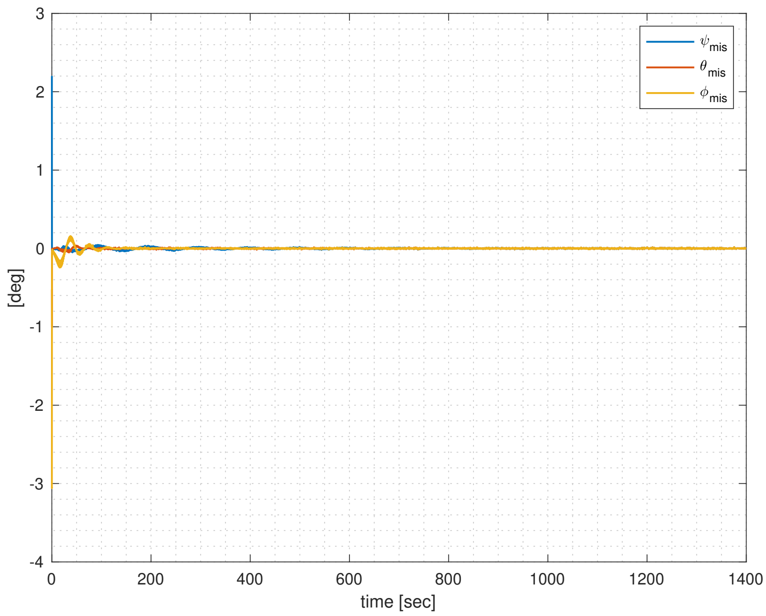

Figure 4.13: Case 1: Star tracker misalignments estimation SMO

$$Mis = \begin{bmatrix}\psi_{mis} & \theta_{mis} & \phi_{mis}\end{bmatrix} = \begin{bmatrix}3.8^\circ & 0.4^\circ & -0.2^\circ\end{bmatrix} \cdot 10^{-4} \tag{4.7}$$

EKF also reach the same magnitude of accuracy but its estimates vary much more than with SMO.

4.1.2 Case 2 - Large attitude rate initial error with small offset

The second case of study is a simulation where the initial conditions of the dynamics are set to a casual orientation for attitude and a high attitude rate:

$$\begin{aligned} \mathbf{q}(0) &= \begin{bmatrix} 0.2 & 0.3 & 0.6 & 0.8 \end{bmatrix}' \\ \boldsymbol{\omega_B}(0) &= \begin{bmatrix} 0.2 & 0.2 & 0.2 \end{bmatrix}' \end{aligned} \tag{4.8}$$

while the filters' and SMO's are:

$$\begin{aligned} \mathbf{q}_{smo}(0) =& \mathbf{q}_{KF}(0) = \mathbf{q}_{EKF}(0) = \begin{bmatrix} 0 & 0 & 0 & 0 \end{bmatrix}' \\ \boldsymbol{\omega_B}_{smo}(0) =& \boldsymbol{\omega_B}_{KF}(0) = \boldsymbol{\omega_B}_{EKF}(0) = \begin{bmatrix} 0 & 0 & 0 \end{bmatrix}' \end{aligned} \tag{4.9}$$

Given the initial conditions, the attitude and attitude rate estimation results are reported in Fig 4.16, Fig 4.17 and Fig 4.18.

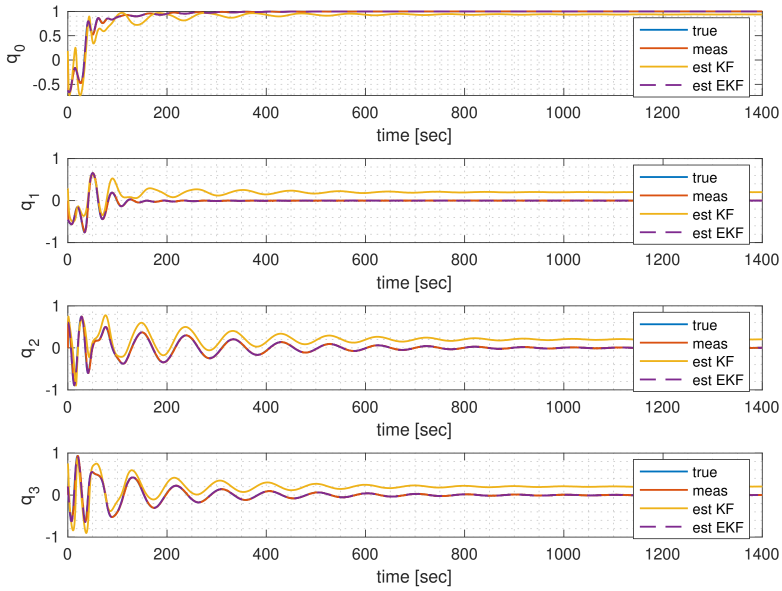

Figure 4.14: Case 2: Quaternions estimation trough KF + EKF

From the previous figures it's evident how the performance of the algorithms decrease when a larger error is considered for the angular rates. In particular for the KF where none of the quaternion component converges to its real value. Instead, in the first case simulation, every quaternion component converged to its real value and only a minimum relevant offset was shown by θ.

Checking the errors without the KF data, it appears that while the linear Kalman filter solutions are not reliable anymore, EKF e SMO are still able to converge at the

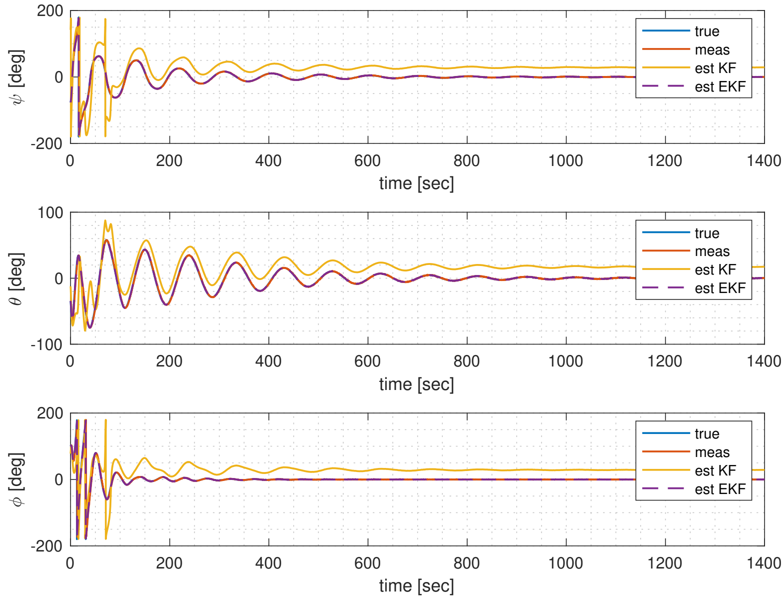

Figure 4.15: Case 2: Attitude estimation trough KF + EKF

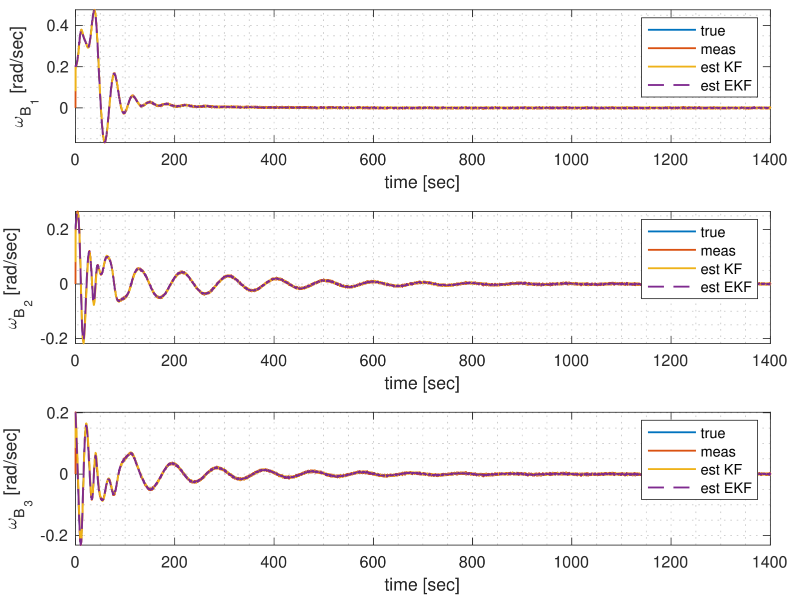

Figure 4.16: Case 2: Attitude rates estimation trough KF + EKF

real states. In particular the observer estimates reach roughly the same accuracy of the first case, while the EKF's get slightly worse as reported in Fig 4.20.

Finally it's possible to evaluate the sensors misalignments with the current estimations from EKF and SMO, reported in Fig 4.21 and Fig 4.22, respectively.

Kalman filter estimates have not been reported since the algorithm does not

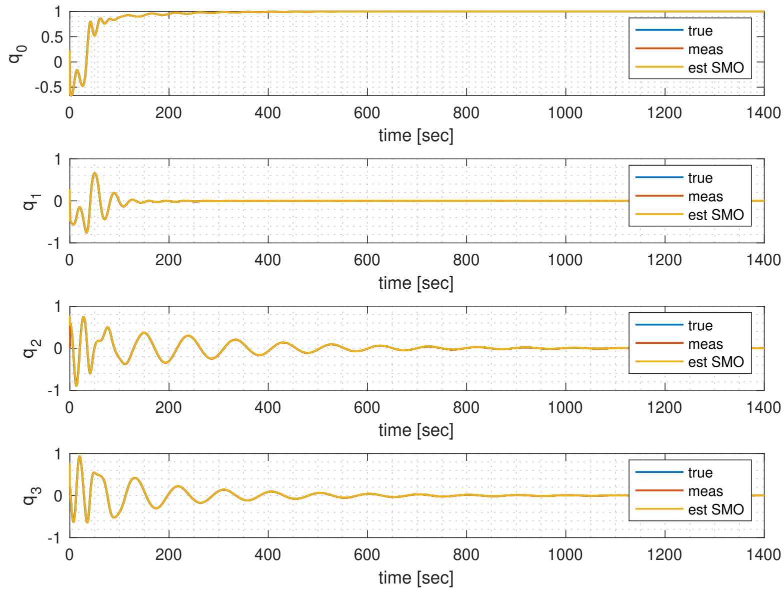

Figure 4.17: Case 2: Quaternions estimation trough SMO

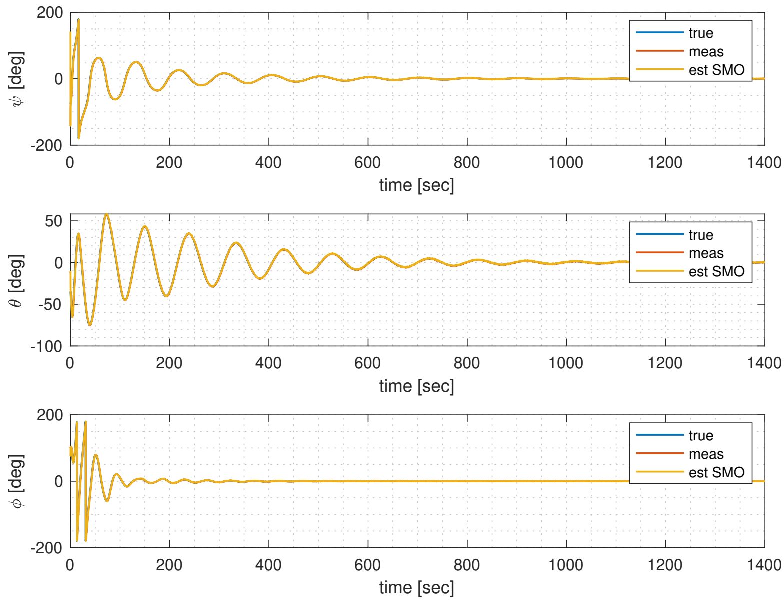

Figure 4.18: Case 2: Euler angles estimation trough SMO

converge if initialized with large attitude rate values.
Again, the EKF results to be still less stable at steady state. However EKF accuracy reaches a range of $\pm 10^{-4}$ while the SMO estimates' ranges from $3.5 \cdot 10^{-3}$ *to* $4 \cdot 10^{-3}$. Thus, in case of large attitude rate initialization, EKF misalignments estimates should be more reliable.

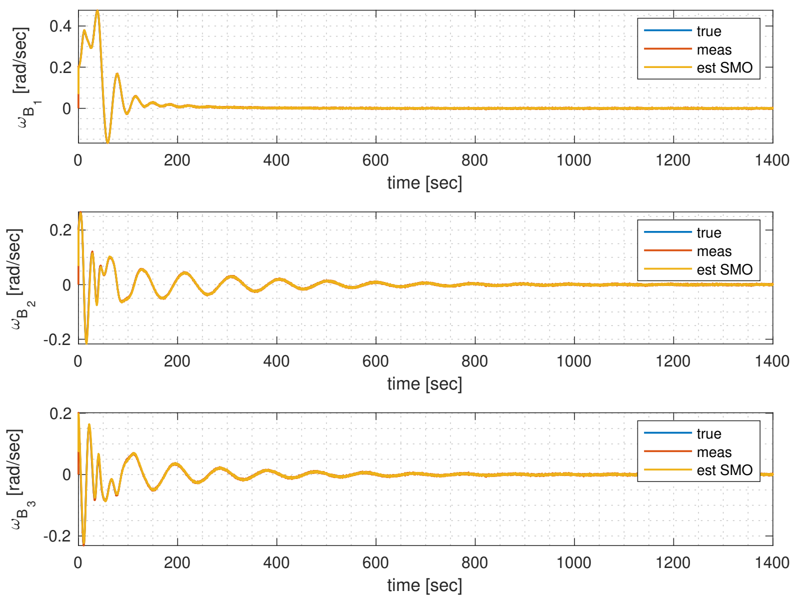

Figure 4.19: Case 2: Attitude rates estimation trough SMO

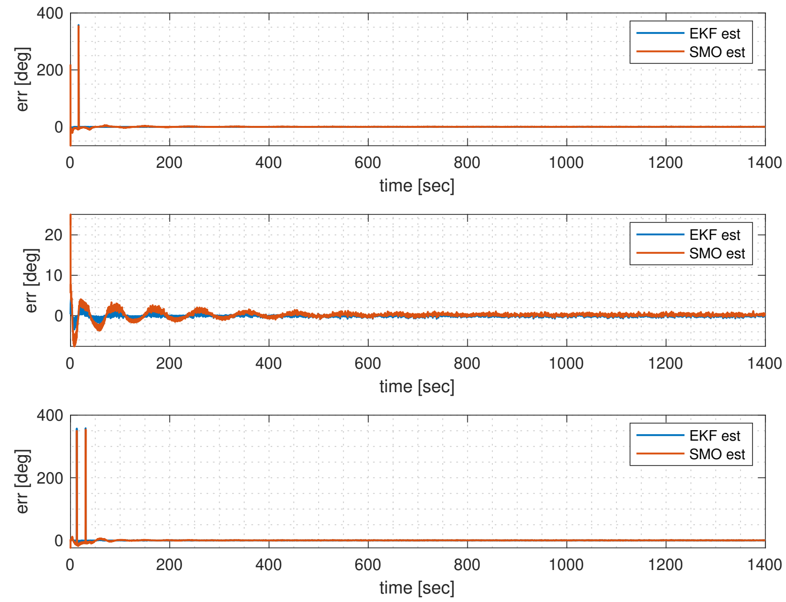

Figure 4.20: Case 2: Attitude errors EKF + SMO

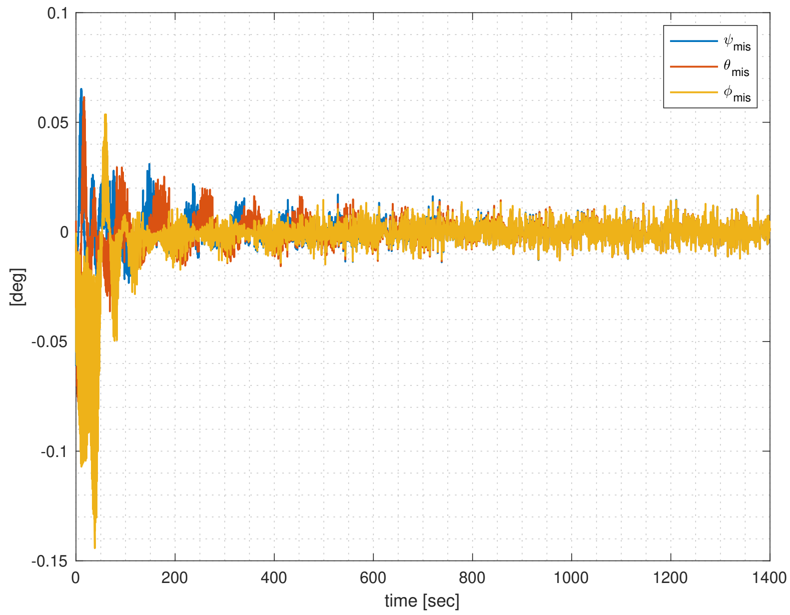

Figure 4.21: Case 2: Star tracker misalignments estimation EKF

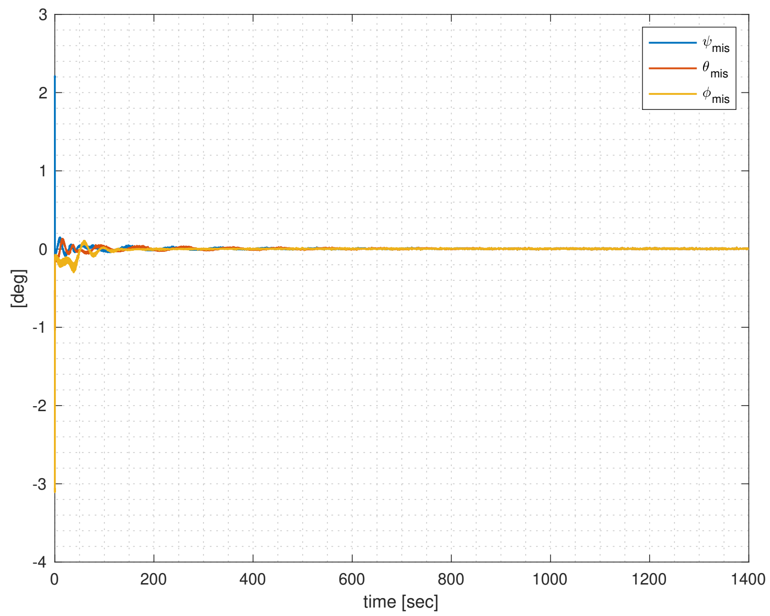

Figure 4.22: Case 2: Star tracker misalignments estimation SMO

4.1.3 Case 3 - Large attitude rate initial error with large offset

In the first two cases, the filters performance have been tested with a random quaternion initialization for both, and small and high attitude rates initialization for the first and second case, respectively. It resulted that with larger initial conditions for the attitude rate the filters converge with more difficulty.

For this reason a further simulation is presented. This case is initialized with the same attitude and attitude rates of case 2, but a much larger star tracker error is introduced. In particular, for the first two cases an error with zero mean and with dozens of arc-seconds as variance has been implemented. In this third case the variance is set to be more than 50 times larger of the previous.
This simulation attempts to replicate the calibration routine performance in presence of large misalignments, caused for example by an errate sensors integration during the assembly phase, besides the smaller offsets caused by vibrations and thermal excursions.

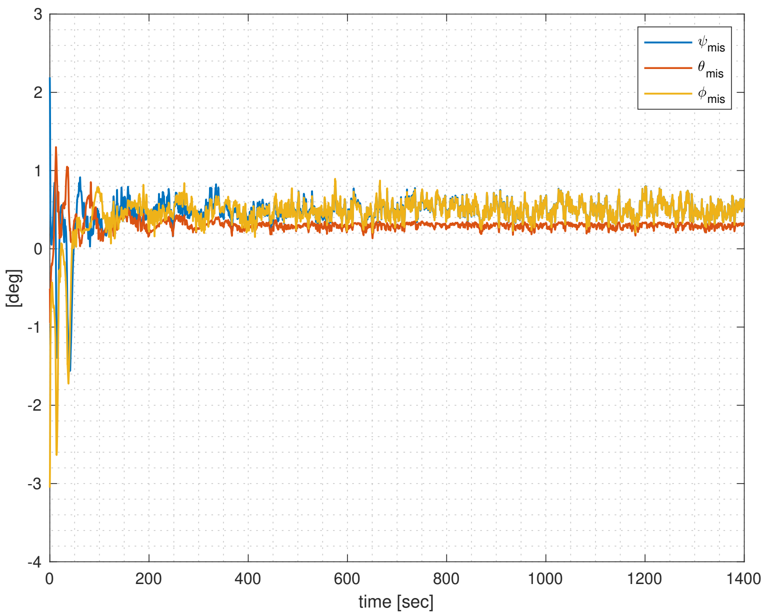

Figure 4.23: Case 3: Star tracker misalignments estimation EKF

In presence of large misalignments, the star tracker mounting errors is obviously bigger than before, but the uncertainty is also higher since a larger disturbance has been introduced in the filter model.
Misalignments estimation from KF, EKF, and SMO are in Fig 4.23, Fig 4.24 and Fig 4.25 respectively.

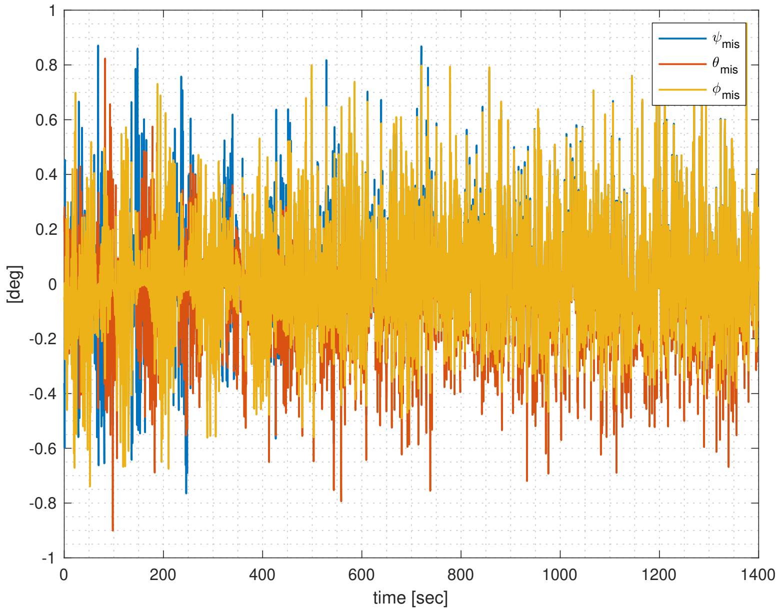

Figure 4.24: Case 3: Star tracker misalignments estimation EKF

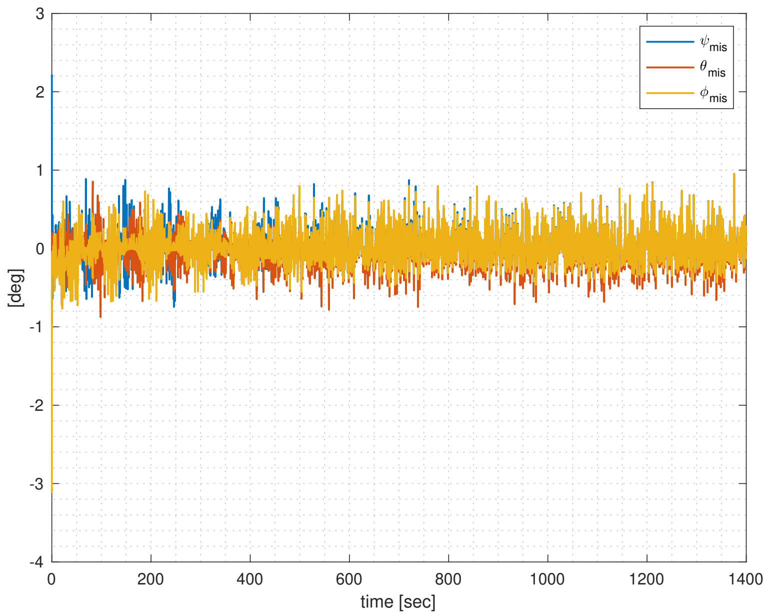

Figure 4.25: Case 3: Star tracker misalignments estimation SMO

Chapter 5

Conclusions

5.1 Simulations summary

Three different algorithms for attitude and body rate with a combination of measurements from star trackers and gyros have been simulated in the S/C modeling environment. The estimators' models have been designed including the spacecraft dynamics, besides the kinematic relations and the simulation's environment includes every major disturbance a LEO spacecraft experiences.
The linear Kalman filter is the one with the lower quality results: in presence of large maneuvers where the nonlinear nature of the system drives the S/C dynamics its estimates are some orders of magnitude lower than for EKF and SMO.
Its nonlinear extension, named EKF, shows exceptional performance in filtering the noise for all the states but a higher execution time than the sliding mode based observer, due to the Jacobian matrices calculations. The EKF weakness consists in its uncertainty when tracking some states in presence of unknown torques and unmodeled dynamics. Indeed, even if the results are sometimes more accurate, a larger magnitude of error oscillation is present as compared to the SMO observer's results.
On the other hand, SMO features a larger amount of noise in the estimation error but manage to drive the estimation error close to zero with some residuals. Globally, the Extended Kalman filter and the Sliding Mode Observer resulted to be less sensitive to measurement noise levels and more robust against uncertainties and input disturbances, respectively.

Besides the algorithms implementation, gain and sliding surfaces tuning have also been performed to increase the results' accuracy. Several initial simulations have been conducted to define the reported values.
Each of the estimates from filters and observer has then been used to track the star sensors misalignments w.r.t the nominal mounting orientation. The attitude estimates' accuracy have shown to directly affect the star trackers offset angles

solutions. In this case a calibration algorithm should rely on accurate attitude estimates to determine if the spacecraft measured orientation does not match the expected measured quaternion.
However, the extended Kalman Filter remains one of the most used, in its multiple forms, for the great majority of spacecraft on board computers. It's relatively simplicity, ease of implementation and flexibility guarantee good performance for in-orbit applications, while degrading in presence of highly nonlinear dynamics or measurement models or for lacking of a good *a priori* estimate. An initial good estimate is thus needed to provide convergence of the filter, even if the future of powerful processors with mass and volume constraints will drive to an autonomous on-orbit reinitialization of the attitude estimation filters.

5.2 Future Work

Future improvements of this thesis work are listed below:

Since the implemented ADCS system does not account for internal torques and structure flexibility, a finite element analysis should be performed to extract the vehicle's natural frequencies and modal shape, allowing for the development of a complete elastic model and improving of the attitude simulation accuracy. This is particularly important for complex body spacecraft, such as Space Rider, where these aspects could really modify the effective response to external and internal disturbances.

The effectiveness of the implemented algorithms for attitude estimation in order to estimate star trackers' misalignments are far to be considered stable. Such a property should be entitled only after a much larger and comprehensive data set employed to conduct simulations. All possible initial conditions, in particular the ones leading to large attitude maneuvers should be considered.

Attitude control system has been implemented as a controller with continuous thrust delivered by some reaction system. In reality this thrust should be modulated trough some width-frequency monitoring relay and applied as discrete torque on the spacecraft. Moreover, if reaction wheel systems are used, the accumulating angular momentum changes the overall S/C momentum and should be included in the system's dynamic. With this kind of system, angular momentum discharging should also be modeled.

In this thesis, orbital dynamics have been completely discarded, assumed to be independent from attitude dynamics. In reality there are multiple effects caused by the dynamics coupling to be considered. Moreover a more accurate modeling of external disturbances needs to receive orbital position data to correctly evaluate particular torques, such as solar pressure and aerodynamic drag.

Numerical simulations have shown the SMO to be stable and accurate over a wide range of initial conditions. One area of future research could be to compare the computational request of the SMO under the additive and multiplicative quaternion corrections, alone and w.r.t. the EKF results.

Since the gains tuning is one of the main drawbacks of the SMO, another future research could develop a neural network to perform optimizations of certain parameters during tuning.

Bibliography

[1] NASA. Hubble space telescope and chandra x-ray observatory.

[2] Jon A Holtzman, J Jeff Hester, Stefano Casertano, John T Trauger, Alan M Watson, Gilda E Ballester, Christopher J Burrows, John T Clarke, David Crisp, Robin W Evans, et al. The performance and calibration of wfpc2 on the hubble space telescope. *Publications of the Astronomical Society of the Pacific*, 107(708):156, 1995.

[3] Martin C Weisskopf, Harvey D Tananbaum, Leon P Van Speybroeck, and Stephen L O'Dell. Chandra x-ray observatory (cxo): overview. In *X-Ray Optics, Instruments, and Missions III*, volume 4012, pages 2–16. International Society for Optics and Photonics, 2000.

[4] F Landis Markley and John L Crassidis. *Fundamentals of spacecraft attitude determination and control*. Springer, 2014.

[5] James R Wertz. *Spacecraft attitude determination and control*, volume 73. Springer Science & Business Media, 2012.

[6] Leonard A McGee, Stanley F Schmidt, Leonard A Mcgee, and Stanley F Sc. Discovery of the kalman filter as a practical tool for aerospace and. In *Industry," National Aeronautics and Space Administration, Ames Research*. Citeseer, 1985.

[7] James Lawrence Farrell. Attitude determination by kalman filtering. *Automatica*, 6(3):419–430, 1970.

[8] James E Potter and WE VANDER VELDE. Optimum mixing of gyroscope and star tracker data. *Journal of Spacecraft and Rockets*, 5(5):536–540, 1968.

[9] Eugene Lefferts, Landis Markley, and Malcolm Shuster. Kalman filtering for spacecraft attitude estimation. *Journal of Guidance, Control, and Dynamics*, 5, 02 1982.

[10] Brian DO Anderson and John B Moore. The kalman-bucy filter as a true time-varying wiener filter. *IEEE Transactions on Systems, Man, and Cybernetics*, (2):119–128, 1971.

[11] Mark E Pittelkau. Survey of calibration algorithms for spacecraft attitude sensors and gyros. *Adv. Astronaut. Sci.*, 129:651–706, 2008.

[12] Dave Bayard. An overview of the pointing control system for nasa's space infra-red telescope facility (sirtf). In *AIAA Guidance, Navigation, and Control*

Conference and Exhibit, page 5832, 2003.

[13] Edward Wong and William Breckenridge. An attitude control design for the cassini spacecraft. In *Guidance, Navigation, and Control Conference*, page 3274, 1995.

[14] Eric A Wan, Rudolph Van Der Merwe, and Simon Haykin. The unscented kalman filter. *Kalman filtering and neural networks*, 5(2007):221–280, 2001.

[15] John L Crassidis, F Landis Markley, and Yang Cheng. Survey of nonlinear attitude estimation methods. *Journal of guidance, control, and dynamics*, 30(1):12–28, 2007.

[16] Malcolm David Shuster and S D_ Oh. Three-axis attitude determination from vector observations. *Journal of guidance and Control*, 4(1):70–77, 1981.

[17] Grace Wahba. A least squares estimate of satellite attitude. *SIAM review*, 7(3):409–409, 1965.

[18] Gerald M Lerner. Three-axis attitude determination. *Spacecraft attitude determination and control*, 73:420–428, 1978.

[19] Marco Lovera, Eliana De Marchi, and Sergio Bittanti. Periodic attitude control techniques for small satellites with magnetic actuators. *IEEE Transactions on Control Systems Technology*, 10(1):90–95, 2002.

[20] Naeem Khan, Sajjad Fekri, Rihan Ahmad, and Dawei Gu. New results on robust state estimation in spacecraft attitude control. In *2011 50th IEEE Conference on Decision and Control and European Control Conference*, pages 2393–2398. IEEE, 2011.

[21] Yaguang Yang and Zhiqiang Zhou. Spacecraft dynamics should be considered in kalman filter attitude estimation. In *AAS/AIAA Space Flight Mechanics Meeting*, number NF1676L-22885, 2016.

[22] Vadim Utkin. Variable structure systems with sliding modes. *IEEE Transactions on Automatic control*, 22(2):212–222, 1977.

[23] Sergey V Drakunov and Vadim I Utkin. Sliding mode control in dynamic systems. *International Journal of Control*, 55(4):1029–1037, 1992.

[24] J-JE Slotine, J Kand Hedrick, and Eduardo A Misawa. On sliding observers for nonlinear systems. 1987.

[25] EA Misawa and JK Hedrick. Nonlinear observers—a state-of-the-art survey. 1989.

[26] James H McDuffie and Yuri B Shtessel. A de-coupled sliding mode controller and observer for satellite attitude control. In *Proceedings The Twenty-Ninth Southeastern Symposium on System Theory*, pages 92–97. IEEE, 1997.

[27] IA Schkolnikov, YB Shtessel, P Zarchan, and DP Lianos. Sliding mode observers versus kalman filter in the homing loop. Technical report, ALABAMA UNIV IN HUNTSVILLE DEPT OF ELECTRICAL AND COMPUTER ENGINEERING, 2001.

[28] K Koprubasi and M-WL Thein. Spacecraft attitude and rate estimation using sliding mode observers. In *International Conference on Recent Advances*

in Space Technologies, 2003. RAST'03. Proceedings of, pages 165–170. IEEE, 2003.

[29] S Salcudean. A globally convergent angular velocity observer for rigid body motion. *IEEE transactions on Automatic Control*, 36(12):1493–1497, 1991.

[30] ESA. A reusable unmanned space transportation system: Space rider.

[31] Jon S. Berndt and Agostino De Marco. Jsbsim reference manual.

[32] Nicoletta Bloise, Elisa Capello, Matteo Dentis, and Elisabetta Punta. Obstacle avoidance with potential field applied to a rendezvous maneuver. *Applied Sciences*, 7:1042, 10 2017.

[33] Wigbert Fehse. *Automated rendezvous and docking of spacecraft*, volume 16. Cambridge university press, 2003.

[34] James Diebel. Representing attitude: Euler angles, unit quaternions, and rotation vectors. *Matrix*, 58(15-16):1–35, 2006.

[35] Bong Wie. *Space vehicle dynamics and control.* Aiaa, 1998.

[36] Yaguang Yang. *Spacecraft Modeling, Attitude Determination, and Control: Quaternion-Based Approach.* CRC Press, 2019.

[37] Anton H De Ruiter, Christopher Damaren, and James R Forbes. *Spacecraft dynamics and control: an introduction.* John Wiley & Sons, 2012.

[38] James R Wertz, David F Everett, and Jeffery J Puschell. *Space mission engineering: the new SMAD.* Microcosm Press, 2011.

[39] CIRA-2012 International Working Group et al. Cospar international reference atmosphere 2012 (cira-2012)–models of the earth's upper atmosphere. *Version*, 1:31, 2012.

[40] George Y Lou. *Models of earth's atmosphere (90 to 2500 km)*, volume 8021. National Aeronautics and Space Administration, 1973.

[41] Arthur Gelb. *Applied optimal estimation.* MIT press, 1974.

[42] Peyman Setoodeh, Alireza Khayatian, and Ebrahim Farjah. Attitude estimation by separate-bias kalman filter-based data fusion. *Journal of Navigation - J NAVIG*, 57, 05 2004.

[43] Yuri Shtessel, Christopher Edwards, Leonid Fridman, Arie Levant, et al. *Sliding mode control and observation*, volume 10. Springer, 2014.

[44] Leonardo. Spacestar - star tracker architecture.

[45] AVIO. Space rider sensor configuration.

[46] Mark E Pittelkau. General definition of relative misalignment. *The Journal of the Astronautical Sciences*, 57(1-2):191–205, 2009.

[47] Kai Xiong, Tang Liang, and Lei Yongjun. Multiple model kalman filter for attitude determination of precision pointing spacecraft. *Acta Astronautica*, 68(7-8):843–852, 2011.